

The effect of localized laser treatment on the microstructure and the corrosion behavior of Fe-Ni-C steel



C.H. Chou

The effect of localized laser treatment on
the microstructure and the corrosion behavior
of Fe-Ni-C steel
by
Chan Hung Chou



Master of Science
in Material Science and Engineering
at the Delft University of Technology,
to be defended publicly on November 24th, 2021, at 09:00 AM.

Thesis committee:

Dr. Y. Gonzalez Garcia, TU Delft, supervisor

Dr. J. Hidalgo Garcia, TU Delft, supervisor

Dr. S. E. Offerman, TU Delft

Preface & Acknowledgement

This thesis investigates the corrosion behavior of a Fe-25Ni-0.2C alloy, which has a reverted austenite/martensite microstructure created by localized laser treatment. This work was carried out to fulfill the requirements for a Master of Science at the Delft University of Technology in the period of February 2020 to November 2021.

This project was initiated by a discussion with Prof. Yaiza Gonzalez Garcia, who was the supervisor of my internship, and I am grateful for the opportunity to have her again as the supervisor of my master thesis. This project is extended into the aspect of corrosion from previous research about the effect of localized laser treatment on the microstructure of steel conducted by Dr. Javier Hidalgo Garcia, who also provides excellent supervision for this work. Many thanks are due to both of them, for the time, in-depth guidance, and patience throughout the entire master project.

In addition, I would like to express my gratitude to various people at the materials science laboratories at TU Delft who are involved in this study, for their guidance and help regarding the experimental setup and materials characterization. Firstly, I would like to thank Sander van Asperen and the lab assistances for the help with the sample preparation and microstructure characterization. Secondly, I would like to thank Agnieszka Kooijman for the guidance on all the corrosion experiments and analysis. Thirdly, I would like to thank Jurriaan van Slingerland for helping me with the laser treatment.

In the end, I'd like to extend my gratitude to my family, girlfriend, and friends, for the love and support.

C.H. Chou

November 2021

Abstract

Laser surface treatment shows great potential to locally create distinct phases in martensitic steels due to its highly localized laser heat flux. Architected materials with microstructures of metastable austenite/martensite phases exhibit advanced mechanical properties, such as a better combination of strength and ductility. In addition, the presence of laser-reverted austenite in martensitic microstructure improves the pitting corrosion behavior due to the better corrosion resistance of austenite over the martensite phase. However, the combined microstructure of different phases might lead to the emergence of galvanic corrosion, which deteriorates the general corrosion behavior of the laser-treated materials. These findings suggest that the laser surface treatment affects the general and the localized corrosion behavior differently, which is an interesting prospect that requires further investigation.

Fe-25Ni-0.2C, the material in this study, has the starting martensite formation temperature (M_s) below room temperature due to its high nickel percentage, which is thermodynamically possible to form reverted austenite and remain austenite phases during laser treatment. In this study, a high-power Nd:YAG laser system is utilized to locally create an austenitic region in a cryogenically-formed martensitic Fe-25Ni-0.2C alloy. Optical microscope (OM) and scanning electron microscope (SEM) are used to assess the microstructure prior to and after laser treatment. The observed microstructure is related to the high spatial gradients in peak temperature and the heating rate of localized laser treatment, which governs the formation mechanisms. Moreover, the effect of laser processing parameters, such as laser power (P) and scanning speed (v), on the laser-affected zone (LAZ) is also investigated.

The corrosion behavior is characterized by potentiodynamic polarization tests in a 3.5% NaCl solution. The corroded surface is examined by optical microscope (OM) and the three-dimensional depth measurement of the pit morphology. In this work, both the general and the pitting corrosion behavior are discussed. The results are influenced by the microstructure created by different heat treatments. The effect of localized laser treatment on the corrosion behavior is investigated on a combined microstructure of laser-reverted austenite/bulk martensite, which has a surface fraction of laser-reverted austenite up to nearly 53%.

Content

Introduction	1
1.1. Motivation.....	1
1.2. Research Questions.....	2
1.3. Outline	2
2. Literature Review	3
2.1. Laser Surface Treatment.....	3
2.1.1. Effect of Laser on Heat Transfer and Microstructure	6
2.2. Process Parameters	7
2.2.1. Laser System	7
2.2.2. Laser Power (P) and Scanning Speed (v).....	7
2.2.3. Focal Position	9
2.3. Phase in Fe-Ni-C.....	9
2.3.1. Austenite Phase	9
2.3.2. Martensite Phase.....	10
2.3.2.1 Morphology of Martensite.....	11
2.3.3. Reversed transformation.....	12
2.4. Corrosion Behavior of Fe-Ni-C Steel.....	12
2.4.1. Pourbaix Diagram of Fe-Ni Alloys in Water	12
2.4.2. Localized Corrosion-Pitting	14
2.4.3. Effect of Nickel Content on Corrosion Behavior of Fe-Ni Alloys.....	15
2.4.4. Effect of Phases on Corrosion Behavior of Steels	16
3. Materials and Methodology	18
3.1. Material and Initial Heat Treatment	18
3.2. Laser Heat Treatment	19
3.3. Sample Preparation.....	20
3.4. Microstructure Characterization	21
3.5. Corrosion Analysis	21
4. Results and Discussion	22
4.1. Effect of Heat Treatment on Microstructure	22
4.2. Effect of Laser Parameters on LAZ and transformation mechanism	23
4.3. Corrosion Behavior of Fe-25Ni-0.2C	28
4.3.1. Open-Circuit Potential (OCP) Analysis	28

4.3.2.	Potentiodynamic Polarization Curves	30
4.3.3.	Surface Morphological Examination after Corrosion Test	34
4.3.4.	Scanning Electron Microscope (SEM)-Energy Dispersive X-ray Spectroscopy (EDS)	39
5.	Conclusion	46
6.	Recommendation	48
7.	Bibliography	49

List of Figures

Figure 2.1 Laser processing diagram: correlation of processing parameters (laser power and laser scanning speed) and laser surface application [15]	4
Figure 2.2 Schematic of laser cladding process of Ti ₆ Al ₄ V/TiC [24]	4
Figure 2.3 Schematic of selective laser melting process (i) selective area of the powder bed melted by laser (ii) scanning process repeated layer by layer (iii) loose powder removed [23]	5
Figure 2.4 Sketch of the keyhole welding [25]	5
Figure 2.5 Correlation between laser absorption and beam wavelength for different metals reprinted from Zanarin [36].	8
Figure 2.6 Schematic diagram of the focal position	8
Figure 2.7 Fe-Ni phase diagram [37]	10
Figure 2.8 The chemical free energies of austenite and martensite as a function of temperature [41]	11
Figure 2.9 Transformation temperature of Fe-Ni-C as a function of heating rate [45]	11
Figure 2.10 Pourbaix diagram for (a) iron, (b) nickel in water system and (c) water (at 25 °C; versus standard hydrogen electrode (SHE)) [48]	13
Figure 2.11 The Fe–Ni composite Pourbaix diagram at 298K in water system (at 25 °C; versus standard hydrogen electrode (SHE)) [49]	14
Figure 2.12 Generic schematic of pitting corrosion [52]	15
Figure 3.1 Equilibrium phase diagram of Fe-25Ni with different carbon content [59]	18
Figure 3.2 Optical images of the top surface (upper) and cross-section (lower) of laser line 8 on as-quenched martensite	20
Figure 3.3 Schematic of tested surface of lasered specimens in corrosion analysis (Dark grey triangles: indentation of hardness test for positioning the LAZ)	20
Figure 4.1 Optical microscopy images of (a) austenite, (b) martensite and (c) tempered martensite specimens	22
Figure 4.2 SEM images of (a) as-quenched martensite (b) tempered martensite	23
Figure 4.3 The optical images of cross-sectioned LSRM-line 8 showing different zones of melt, LAZ and parent martensite	24
Figure 4.4 Optical microscopy images of laser lines 1 to 8 on as-quenched martensite, which corresponds to (A) to (H), respectively (Etchant: line 1-4: Nital 2%; line 5-8: waterless Kalling)	25
Figure 4.5 SEM micrographs of the melting zone of LSRM-line 8	26
Figure 4.6 Optical microscope images of laser affected zone (etched with waterless Kalling)	26
Figure 4.7 Grain structure in LAZ (fine-grained austenite: straight grain boundary; coarse-grained austenite: wavy grain boundary)	28
Figure 4.8 The open-circuit potential (OCP versus Ag/AgCl) with time 3.5 % NaCl solution	29

Figure 4.9 Polarization curves of all specimens in 3.5 % NaCl solution (vs. Ag/AgCl)	31
Figure 4.10 Schematic of galvanic couplings of lasered martensite (white scheme at bottom left corner: a simplified representation of bulk microstructure of austenite and butterfly martensite)	34
Figure 4.11 Optical microscope images and their corresponding depth color maps of surface of (a) austenite, (b) martensite and (c) tempered martensite specimens after potentiodynamic polarization test in 3.5% NaCl	36
Figure 4.12 Optical microscope images and their corresponding depth color maps of surface of (a) lasered martensite and (b) lasered tempered martensite after potentiodynamic polarization test in 3.5% NaCl	38
Figure 4.13 SEM micrograph of the pit on the martensite surface after potentiodynamic polarization test in 3.5% NaCl, and its corresponding EDS profile of inside-the-pit (marked as green cross) and the surface position (marked as orange cross)	39
Figure 4.14 SEM micrograph of residual NaCl salts deposited on the surface after potentiodynamic polarization test in 3.5% NaCl, and its corresponding EDS profile	41
Figure 4.15 SEM micrograph of the surface of martensite after potentiodynamic polarization test in 3.5% NaCl, and its corresponding EDS profile	41
Figure 4.16 (a) SEM micrograph of the surface of austenite after potentiodynamic polarization test in 3.5% NaCl (b) Higher-magnification SEM micrograph of the area (marked with blue dashed line) and its corresponding EDS profile	43
Figure 4.17 (a) and (b) SEM micrographs of the two pits of lasered martensite after potentiodynamic polarization test in 3.5% NaCl, and its corresponding EDS profile	44
Figure 4.18 SEM micrograph of the pit of lasered tempered martensite after potentiodynamic polarization test in 3.5% NaCl, and its corresponding EDS profile	45
Figure 4.19 Schematic of pitting corrosion of martensite specimen (no corrosion products on the pit all)	45
Figure 4.20 Schematic of pitting corrosion of lasered martensite specimen (corrosion products on the pit all)	45

List of Tables

Table 2.1 Morphology and crystal orientation of different types of martensite in Fe-Ni-C [44]	11
Table 3.1 Alloy composition	18
Table 3.2 Laser parameters setting	20
Table 4.1 The mean OCP for each specimen in 3.5 % NaCl solution at 600th second	29
Table 4.2 Mean values of parameters (\pm standard deviation) from polarization curves in 3.5 % NaCl solution (vs. Ag/AgCl)	32
Table 4.3 Pitting corrosion parameters for all specimens	35
Table 4.4 Corresponding weight percentages of elements detected in Figure 4.13	40
Table 4.5 Corresponding weight percentages of elements detected in Figure 4.15	42
Table 4.6 Corresponding weight percentages of elements detected in Figure 4.16 (b)	43
Table 4.7 Corresponding weight percentages of elements detected in Figure 4.17	44
Table 4.8 Corresponding weight percentages of elements detected in Figure 4.18	45

List of Abbreviations

AES - Auger electron spectroscopy
BCT - body-centered tetragonal
CAD - computer-aided data
EDM - Electrical Discharge Machine
EDS - energy dispersive X-ray spectroscope
EIS - electrochemical impedance spectroscopy
FCC - face-centered-cubic
LAZ - laser affected zone
LC - laser cladding
LSM - laser surface melting
Nd:YAG - neodymium-doped yttrium aluminium garnet
OCP - open-circuit potential
OM - optical microscopy
RA - retained austenite
SECMS - scanning electrochemical microscope
SEM - scanning electron microscopy
SEP - standard electrode potential
SKPFM - scanning Kelvin probe force microscopy
SLM - selective laser melting
SS - stainless steel
TRIP - transformation-induced plasticity
XPS - X-ray photoelectron spectroscopy
XRD - X-ray diffraction

1. Introduction

1.1 Motivation

Architected materials, by the definition from Valdevit et al.[1], are multiphase materials in which the topological distribution of the phases is carefully controlled and optimized for specific functions or properties”. These materials have several advantages, such as optimum strength and stiffness [2] . Particularly, the materials with austenite/martensite phases show a good combination of tensile strength and total elongation [3]. The enhancement in strength and ductility is attributed to the transformation of austenite to martensite during the plastic deformation, which refers to transformation-induced plasticity (TRIP) effect [4]. Conventionally, the production of austenite-martensite dual phase steels requires a cooling medium for quenching, such as water [5]. For certain materials, subsequent immersion in liquid nitrogen is required to induce martensitic transformation [6].

Using laser heat treatment to create architected structure has several advantages over conventional thermal processing, including highly localized, high heating and cooling rates [7]. Laser is used as a heat source where a high energy beam is applied on a highly localized region at the surface while the rest of the component acts as a heat sink. Such a trait enables laser treatment to rapidly heat up and alter the properties of the surface of metal within its penetration depth, without affecting the properties of the bulk material. With localized processed area and the conduction of heat transfer into the bulk material, the rapid cooling rate is achieved without the requirement of an extra cooling medium, which is referred to as self-quenching [8].

Localized laser treatment has been used on martensitic stainless steels to create austenite/martensite microstructure [9]. With high-intensity laser heating the localized region of the surface to above austenitizing temperature, the transformation from the martensite phase to austenite, i.e. reverse transformation, takes place, resulting in a microstructure with a new combination of austenite/martensite. In addition to the beneficial effect on mechanical properties, lasered localized heat treatment exhibits promising outcomes for enhancement of localized corrosion behavior as the pitting potentials shifted in the noble direction [9,10]. This is attributed to the presence of the austenite phase that has a better pitting corrosion resistance than the martensite phase. Moreover, laser treatment leads to the dissolution or redistribution of precipitates or inclusions, leading to a chemical homogenization of the laser-treated materials. The proportion of the retained austenite can be modified by controlling the laser processing parameters [11], such as laser power (P) and scanning speed (v), and hence the pitting corrosion properties of the architected materials.

However, the general corrosion behavior might deteriorate as the galvanic coupling emerges between the laser-treated and untreated surfaces [12], leading to an increase in corrosion rate. At a macro scale, the surface ratio of laser-treated to untreated surfaces, which is an important geometric parameter referred to cathode-to-anode ratio, influences the galvanic corrosion significantly. At a micro scale, the galvanic corrosion might occur between austenite and martensite

phases [13], resulting from the difference in potentials of the two phases that leads to localized corrosion potential gradients or selected phase dissolution.

These findings have suggested that the localized laser treatment can influence the general and localized corrosion through different mechanisms, and it can be an interesting topic that requires further investigation. Fe-25Ni-0.2C alloy is a suitable material for creating an architected microstructure of austenite/martensite phases by localized laser treatment. With a high content of nickel that serves as an austenite stabilizer, Fe-25Ni-0.2C shows a high potential to form reverted austenite from martensite and remain as austenite phase during laser treatment.

1.2 Research Questions

The objective of this thesis is to investigate the possibility of using localized laser treatment to create a distinct region of reverted austenite from a cryogenically formed martensitic Fe-25Ni-0.2C steel, and its effect on the microstructure and corrosion behavior. Based on the objective, the following research questions were formulated:

1. What is the effect of different heat treatments, such as cryogenic and tempering, on the microstructure and the corrosion behavior of Fe-25Ni-0.2C steel?
2. Can localized laser heat treatment be used to create an architected austenite/martensite microstructure on Fe-25Ni-0.2C steel? What are the microstructural characteristics and transformation mechanisms?
3. How do the laser parameters, laser power (P) and scanning speed (v), influence the laser-treated Fe-25Ni-0.2C steel in terms of the microstructure?
4. How does the localized laser treatment affect the general and localized corrosion behavior of Fe-25Ni-0.2C steel? What are the corrosion mechanisms?

1.3 Outline

In the following chapter, the background information is given on the laser treatment and the effect of the laser processing parameters on the microstructure. In addition, the introduction of phase properties along with the transformation mechanisms are explained. At the end of Chapter 2, the mechanisms of the corrosion behavior are introduced. In Chapter 3, the materials and the experimental methods are presented. The results of this study are presented and discussed in Chapter 4, which is subdivided into two main aspects, microstructure and corrosion behavior. In the end, main conclusions are drawn with respect to the research questions. Recommendations are provided based on the setting and findings of this work.

2. Literature Review

In this chapter, a general background on laser surface treatments is first presented, followed by the introduction of heat transfer in materials. The thermal information can be used to understand the formation of microstructures by laser in this work, and the effect of laser processing parameters on microstructures is also provided. The chapter then continues by discussing the phases and the reverse transformation of Fe-Ni alloy, and its corrosion behavior is addressed at the end of this chapter.

2.1 Laser Surface Treatment

In surface engineering, lasers are widely used due to their advantages over the conventional surface treatment, including precision of operation, fast processing, and localized treatment [14]. Laser surface treatment involves heating the surface of the workpiece with a source of coherent electromagnetic radiation, i.e. laser light, in a protective gas atmosphere. Absorption of the laser radiation takes place at the surface of the materials, and in bulk up to the optical penetration depth, which results in modifying only the properties of the surface, such as hardness, toughness and corrosion resistance, leaving the bulk material unaffected.

Depending on the peak surface temperature achieved during the heating, the laser surface treatment can be categorized into three main classes [15]: solid-state transformation treatment (laser surface hardening), laser surface melting and ablation (keyhole welding). In solid-state transformation treatment on steels, the surface of the workpiece typically heats up to the austenite temperature region (above A_1 temperature), but not above the melting temperature, and cools down rapidly due to self-quenching to form the martensite phase, leading to an improvement in the hardness, wear [16], erosion [17] and corrosion resistance [18, 19]. Self-quenching refers to the process of heat spreading from the laser focal spot evenly in all directions in an isotropic solid, which causes high cooling rate, and is the main mechanism for laser surface hardening.

In laser surface melting (LSM), the peak temperature of the surface reaches the melting temperature but not significantly above the vaporization temperature, which can be achieved by further increasing the laser power (P) or decreasing the scanning speed, as shown in Figure 2.1 [15], causing melting of the material and subsequent rapid cooling, and leads to the surface modification, such as dissolution of precipitates, refinement of microstructure, and chemical homogenization [20]. Kwok et al. [9] investigated the effect of laser surface melting on corrosion behavior of martensitic stainless steels, and found out that it significantly improved the pitting corrosion resistance by shifting the pitting potential to a more noble direction. The enhancement of pitting corrosion was mainly attributed to the refinement or dissolution of carbides from the boundaries into the grains caused by laser input energy. Mahmoudi et al. [19] conducted the EDS analysis on revealed that the amount of chromium in the grains increased after laser treatment, indicating the reducing amount and size of chromium-containing carbides at the grain boundaries. Decarburization could be another mechanism contributing to the decreased carbides. Maharjan et al. [21] reported that decarburization occurred during laser surface treatment. The surface was austenitized during the

heating of laser treatment, providing the condition for the reaction between surface carbon and atmosphere, causing carbon to diffuse out. Due to short interaction time during laser treatment and the decreased mobility of carbon caused by alloying elements, the carbon in the bulk material failed to fully replenish the loss of carbon at the surface, resulting in less amount of carbon for carbide formation, and consequently, more passive alloying elements left in solid solution.

Other laser applications, such as laser cladding (LC) [22] and selective laser melting (SLM) [23], also belong to the class of laser surface melting. Laser cladding (LC) is a powder injection technique that rapidly melts and solidifies the feeding material powder as well as a thin layer of the substrate surface with a laser source, forming a metallurgical bond between the cladding materials and the substrate, as illustrated in Figure 2.2 [24]. This application is widely used for rapid manufacturing, component repair, and surface coating; Selective laser melting (SLM) is an additive manufacturing process designed to produce objects from metallic or polymer powder according to computer-aided data (CAD), which uses high-intensity laser power as an energy source to melt and fuse selective area of powder by scanning a powder bed layer by layer, as illustrated in Figure 2.3 [23]. The SLM component provides the advantage of low post-processing cost due to its near-net-shaped property, but has the drawbacks of relatively high surface roughness caused by the balling effect, and crack formation due to the residual stress resulting from the thermal fluctuation of the materials during SLM.

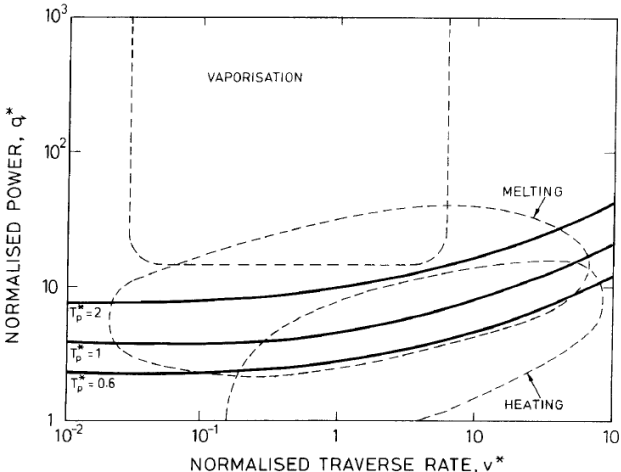


Figure 2.1 Laser processing diagram: correlation of processing parameters (laser power and laser scanning speed) and laser surface application [15]

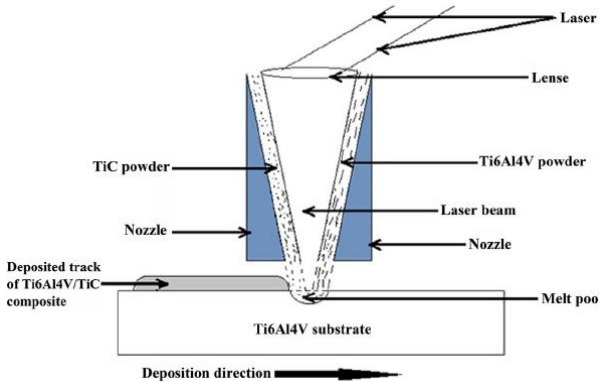


Figure 2.2 Schematic of laser cladding process of Ti_6Al_4V/TiC [24]

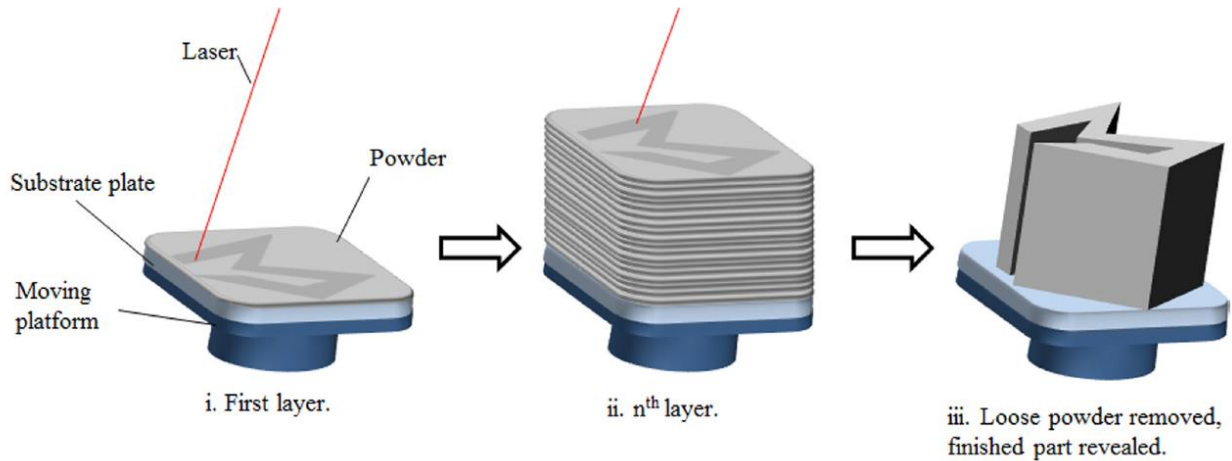


Figure 2.3 Schematic of selective laser melting process (i) selective area of the powder bed melted by laser (ii) scanning process repeated layer by layer (iii) loose powder removed [23]

With further increase in the peak temperature by adjusting the laser power and the scanning speed, the surface temperature reaches the vaporization temperature, T_v , and the vapor pressure (recoil pressure) creates a depression in the melted workpiece, which is referred to the ablation (keyhole welding). This depression experiences a significant absorptivity due to multiple absorption/reflection of the laser beam. It causes higher temperature as well as an increase in the depression, forming of a long and narrow cavity, or keyhole, as shown in Figure 2.4 [25].

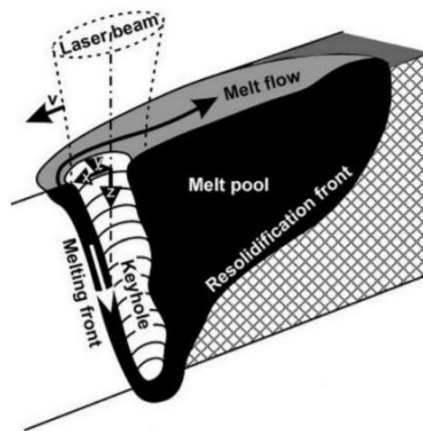


Figure 2.4 Sketch of the keyhole welding [25]

2.1.1 Effect of Laser on Heat Transfer and Microstructure

During the interaction of the laser with solids, a variety of physical processes occur. When electromagnetic radiation strikes the surface of solid material, some part of it is reflected, some absorbed and some transmitted. When the laser beam interacts with a solid surface, the force induced by the electric field causes the electrons in the irradiated region to vibrate. The absorption of electromagnetic energy in metals occurs by photon-electron interactions, which raises the energy state of the electrons. This process of photons being absorbed by electrons refers to the inverse bremsstrahlung effect [26]. If the accelerated electrons re-radiate in all directions, the reflected and transmitted radiation occurs; If electrons undergo several collisions with lattice phonons and transfer some of the electrons excess energy to lattice phonons, the energy is considered absorbed, and the phonons would cause the structure to vibrate. The thermalization time of most metals, i.e. the amount of time for the excited electronic states to transfer energy to phonons and thermalize, is on the order of 10^{-12} – 10^{-10} s [27]. When the laser-induced excitation rate is low in comparison to the thermalization rate, it is considered that the absorbed laser energy is directly transformed into heat. If sufficient energy is absorbed, melting of materials occurs because the vibration of the structure is intensified and the bonding is stretched. The absorptivity of a material is determined by its optical constants n (refractive index) and k (extinction coefficient) which are a function of the materials, the laser wavelength, the temperature and the angle of incident [28].

The governing heat equation for heat transfer in the material can be stated as follows [29]:

$$\rho C_p \frac{\partial T}{\partial t} = k \nabla^2 T \quad (2.1)$$

Where k (W/(m · K)) is the thermal conductivity, a measure of materials ability to conduct. C_p [J/(kg · K)] is the specific heat capacity, and ρ [kg/m³] is the density of the material. With algebraic rearrangement, the heat conduction equation in Cartesian coordinates is obtained:

$$\frac{\partial T}{\partial t} = \alpha \left(\frac{\partial^2 T}{\partial x^2} + \frac{\partial^2 T}{\partial y^2} + \frac{\partial^2 T}{\partial z^2} \right) + \frac{q}{\rho C_p} \quad (2.2)$$

$$, \text{ where } \alpha = \frac{k}{\rho C_p}$$

where α represents thermal diffusivity, which is the thermal conductivity divided by density and specific heat capacity at constant pressure. It is a measure of the ability of a material to conduct thermal energy relative to its ability to store thermal energy. High diffusivity means heat transfers rapidly; q denotes the heat fluxes in the workpiece.

The heat equation governs the heat transfer phenomenon. From previous studies [30] and literature three-dimensional finite element modelling has been conducted to predict stress field [31] and thermal history [30, 32]. The simulation of transient three-dimensional heat transfer in a thin metal plate heated by a moving heat source, which is the same condition as the laser treatment in this work, can accurately predict the effect of laser on the sharp temperature and heating and cooling rate gradients. This can give a valuable insight into the microstructure evolution. Indeed, the final

microstructure at the heat-affected zone showed good agreement with modelling. Besides, the stress field analysis, material dilatation can produce residual stress during the solid-phase transformation from austenite to martensite [31, 33]. The laser affected zone can be tailored by changing the laser parameters. For example, the peak temperature [30, 31, 32] of the material as well as the heating and cooling rate decreases when the distance from the laser focal spot increases. The higher the moving heat source velocity, the faster the temperature changes during both heating and cooling. More details of the effect of laser parameters on the microstructure will be discussed in the following section and the experimental results obtained in this work.

2.2 Process Parameters

In this section, the effect of laser parameters, such as laser system, laser power and scanning speed and focal position, has been investigated with the aim to modify the microstructure of the laser-treated surface, and accordingly the properties.

2.2.1 Laser System

Laser has become a popular method for industrial processing after the invention of carbon dioxide (CO₂) laser back in 1960s [34], a laser system that uses a gas mixture consisting of helium, nitrogen and carbon dioxide as an active medium, which generates laser radiation with a wavelength of 10.6 μm . Carbon dioxide laser is widely used in the application of laser cutting and welding [25] of metal materials. During the laser-material interaction, the absorption of a metal surface strongly depends on the irradiation wavelength, and it increases as the wavelength is short. A solid-state laser system, neodymium-doped yttrium aluminium garnet (Nd:YAG) laser, which has a shorter wavelength of 1.064 μm , emerges as a competitive tool in laser surface treatment.

During the interaction between the laser beam and the material, part of the radiation is absorbed while the rest is reflected. The absorptivity of materials is influenced by the laser wavelengths, which are shown in Figure 2.5. At shorter wavelengths, the more energetic photons can be absorbed by a more significant number of electrons, so the reflectivity drops and the absorptivity of the surface increases. For steel materials, the absorption has significantly improved when the laser system progresses from the molecular CO₂ laser ($\lambda \approx 10.64 \mu\text{m}$) to the solid-state neodymium-doped YAG (Nd:YAG) laser ($\lambda \approx 1.06 \mu\text{m}$).

2.2.2 Laser power (P) and Scanning Speed (v)

Laser power refers to the output of the laser beam, which is measured in the unit of Watts, and controls the amount of energy absorbed into the laser-treated material. As the laser power increases, both the peak temperature and the temperature gradient of the melting zone increase, and accordingly the depth of the melting zone increases [9]. The depth of laser penetration increases with peak energy for pulsed lasers, which can be achieved by increasing the pulse width at constant laser power [18]. When the pulsed energy remained fixed, every decrease in the pulse width would increase the laser peak power, and Mahmoudi found out that the melting of the workpiece only occurred when the pulse width decreased down to a critical value [19].

Laser scanning speed denotes the relative movement of the laser source and the workpiece, determines the time of the laser-material interaction, and hence influences the solidification rate (cooling rate) and the melt pool temperature. When the scanning speed increased, the solidification rate (cooling rate) was higher, while the melt pool peak temperature showed a decreasing trend. Lo et al. [17] studied the effect of the scanning speed, and they found that both the dissolution of carbides and the depth of laser penetration increased with the decreasing laser scanning speed due to a longer interaction time. The same result has been discovered by Mahmoudi [19], in which the amount of Cr in the bulk increased with decreasing laser scanning speed, indicating a higher dissolution of the high-chromium carbides into the bulk with a longer interaction time.

The formation of microstructure during solidification in LSM applications determines the properties of the laser-treated materials, on both mechanical and corrosion scales. With less austenite phase transforming into martensite phase during rapid cooling, which leads to a higher volume fraction of retained austenite (RA), the corrosion behavior improved [9] due to the higher pitting corrosion resistance of austenite over martensite, but the mechanical properties, such as hardness, deteriorates [18]. Thus, controlling this ratio is critical to achieving the desired properties of the materials.

Colaco and Vilar [35] further found that laser processing parameters were critical to alter the proportion of retained austenite, which increased with decreasing power density and increasing scanning speed. By varying the two parameters, the cooling rate became faster during solidification, resulting in microstructural refinement [11], which was further proven experimentally and analytically to decrease the martensite start temperature (M_s), and increase the volume fraction of retained austenite.

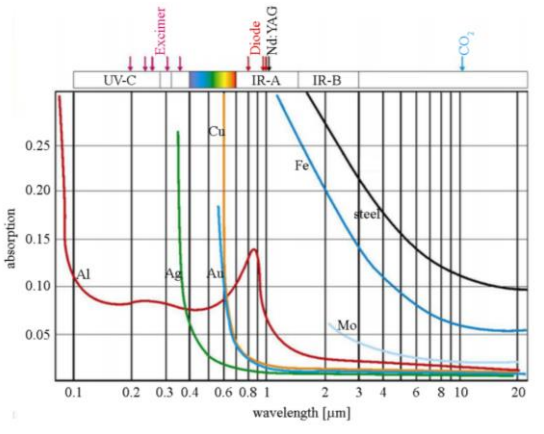


Figure 2.5 Correlation between laser absorption and beam wavelength for different metals reprinted from Zanarin [36].

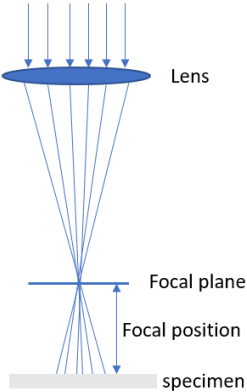


Figure 2.6 Schematic diagram of focal position

2.2.3 Focal Position

Focal position refers to the distance between the laser focal plane and the surface of the workpiece, as shown in Figure 2.6, and exhibits a direct effect on the power density by changing the laser spot size, which influences the depth of the laser-heated zone. By increasing the focal point position, the spot size increased due to the divergence of the laser beam and the power density decreased, leading to less transfer of heat energy to the material, and hence reduced the depth of the laser-heated zone [18].

2.3 Phases in Fe-Ni-C

In this work, austenitic Fe-25Ni-0.2C alloys is first converted into martensitic microstructure by cryogenic treatment, which is followed by local laser treatment to form microstructure with a combination of reverted austenite/ bulk martensite. The introduction of austenite, martensite and the reverse transformation of martensite to austenite upon heating are the main subjects in the following section.

2.3.1 Austenite Phase

Austenite, denoted as γ -phase, is a face-centered-cubic (FCC) iron that is thermodynamically stable above the critical eutectoid temperature (A_1) of around 1000 K (727 °C) in plain steel. With the addition of γ -stabilizer elements, such as carbon and nickel, the critical points of iron are altered by raising the A_4 point (the temperature at which the austenite transforms to the delta iron) and lowering the A_3 point (the temperature at which the ferrite transforms into the austenite), expanding the range in which the austenite phase is stable, as it can be observed in the Fe-Ni diagram [37] in Figure 2.7. At room temperature, austenite phase is thermodynamically unstable, but the driving force for thermodynamic transformation is insufficient, and hence the metastable nature of the austenite. Metastable austenite can transform to martensite either by cooling below martensite start temperature (M_s) (thermal) or by deformation (mechanical). Hence, a critical characteristic of the austenite phase is its stability.

Martensite start (M_s) temperature is a significant parameter to describe the stability of austenite in steels, and it decreases with the increasing content of γ -stabilizer elements [11]. In thermodynamics, the addition of these elements reduces the Gibbs free energy difference between austenite and martensite, i.e. chemical driving force $\Delta G^{\gamma\alpha'}$, and hence the M_s decreases [38]. Carbon shows the strongest effect in reducing the M_s temperature among all the γ -stabilizer. The effect of austenite and carbon content on the martensite start (M_s) temperature of Fe-Ni-C alloys is confirmed by the findings of Maxwell et al. [4]. The M_s temperatures of Fe-Ni-C alloys with high nickel content (more than 20 wt%) and carbon content (up to 0.2wt%) are all below 0 °C.

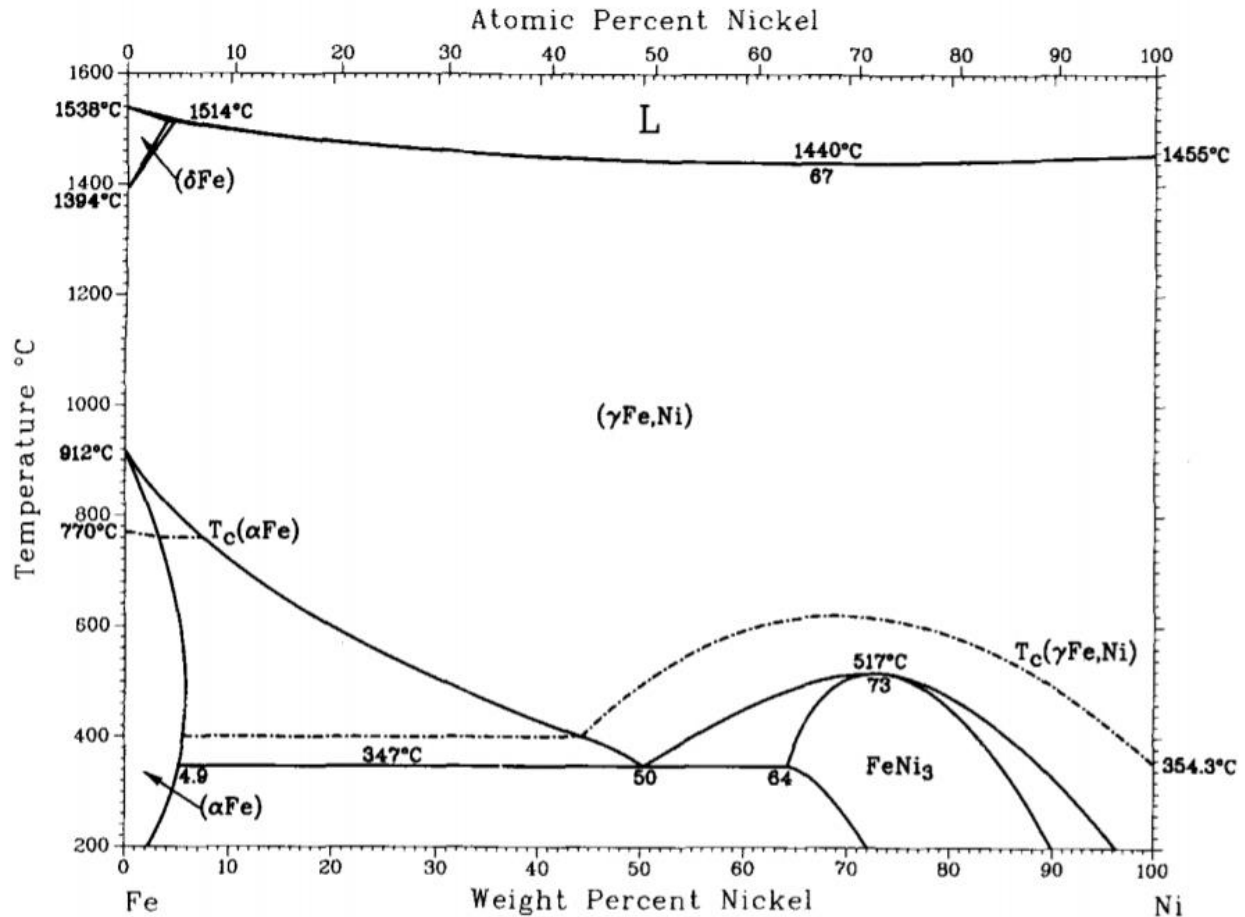


Figure 2.7 Fe-Ni phase diagram [37]

2.3.2 Martensite Phase

Martensite phase (α') transformation is a diffusionless process, i.e. during the transformation individual atomic movements are less than one interatomic spacing, which is achieved by quenching of the austenite phase at a high cooling rate that suppresses the diffusion of carbon atoms out of the crystal structure, forming a highly distorted body-centered tetragonal (BCT) structure that is supersaturated with carbon [39]. The transformation can be thermally or mechanically driven. A certain amount of undercooling ΔT from T_0 (equilibrium temperature; temperature where the chemical Gibbs free energies of austenite and martensite phases are equal) is required for martensitic transformation. Martensitic transformation can take place when the temperature reaches martensite start (M_s) temperature, i.e. the driving force is large enough to overcome the opposing surface and strain energies associated with the formation of a martensite nucleus [40], as shown in Figure 2.8 [41]. The mechanical driving force, U , resulting from an externally applied stress can be complemented to add to the chemical driving force when the undercooling is insufficient for the onset of martensitic transformation.

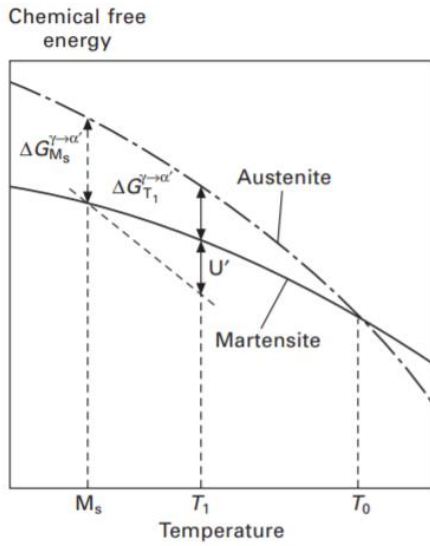


Figure 2.8 The chemical free energies of austenite and martensite as a function of temperature [41]

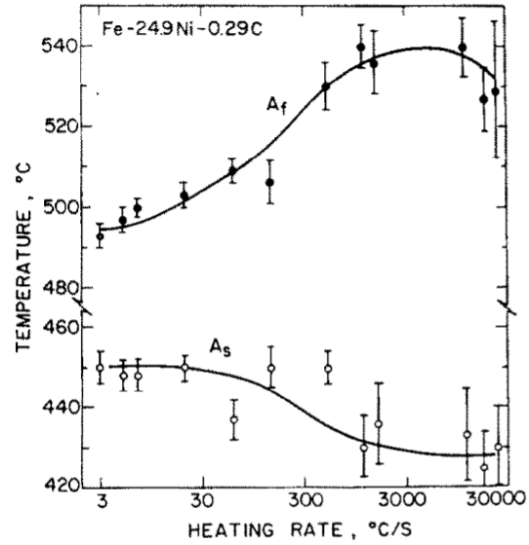


Figure 2.9 Transformation temperature of Fe-Ni-C as a function of heating rate [45]

2.3.2.1 Morphology of Martensite

In Fe-Ni-C alloys, four types of martensite morphologies have been observed, which are lath, butterfly, lenticular and thin plate martensite, and each type exhibits a different crystallographic orientation [42, 43]. The formation of different morphologies is linked to the nickel content in the alloys and its formation temperature, as shown in Table 2.1 [44], and the transition temperature between different morphologies was found to increase with increasing carbon content [43].

Martensite type	Plate	Lenticular	Butterfly	Lath
Shape				
Ni concentration in Fe-Ni alloy	High	High	Low	Low
Formation temperature	Low	Low	High	High
Substructure	Twins	Twins + dislocations	Twins + dislocations	Dislocations
Crystal orientation relationship	G-T	G-T, N-W or K-S	K-S or N-W	K-S
Habit plane	$\{3\ 10\ 15\}_\gamma$	$\{3\ 10\ 15\}_\gamma$ or $\{2\ 5\ 9\}_\gamma$	$\{2\ 2\ 5\}_\gamma$	$\{5\ 5\ 7\}_\gamma$ or $\{1\ 1\ 1\}_\gamma$

Table 2.1 Morphology and crystal orientation of different types of martensite in Fe-Ni-C [44]

2.3.3 Reversed Transformation

Reversed transformation of martensite to austenite takes place during heating up to reverse transformation start temperature, A_s , and finishes at finish temperature, A_f , two critical temperatures of which correspond to A_{c1} and A_{c3} , respectively. For Fe-Ni-C alloys, depending on governing parameters of the chemical composition and the heating rate, the reverse transformation can occur by two mechanisms: diffusional or displacive [45, 46].

In Fe-Ni binary alloys, both the temperatures A_s and A_f are independent of heating rate within the range from $\sim 1 \text{ K s}^{-1}$ to $\sim 8000 \text{ K s}^{-1}$ [46], indicating the displacive mechanism of the reversed transformation with no occurrence of significant rearrangement within the martensite before the start of the transformation. In Fe-Ni-C alloys, with the presence of high-diffusivity carbon, the mechanism is diffusional when carbon contents exceed 0.05% C. At a lower heating rate, the carbon atoms have more time for diffusion, and result in complete carbide precipitation, which decreases the carbon concentration in the parent martensite matrix, leading to an increase in A_s temperature, as shown in Figure 2.9 [45]. The change of A_f temperature from increasing to decreasing trend suggests the alteration of mechanism from diffusional to displacive nature. For the displacive mechanism to take place, the diffusion of carbon needs to be suppressed, which occurs under the condition of low carbon content ($\sim 0.004 \text{ wt\%}$) and very high heating rates (above 1500 K s^{-1}) [45]. In displacive transformation, the process is accompanied by surface relief and a high density of dislocation. Although the reverse transformation is applied for grain refinement, the size, shape and orientation of reverted austenite were identical to initial austenite grains under certain conditions, a phenomenon of which is referred as austenite memory.

2.4 Corrosion Behavior of Fe-Ni-C Steel

The corrosion behavior of Fe-25Ni-0.2C in this work is examined by potentiodynamic polarization in the electrolyte of sodium chloride. In this section, the Pourbaix diagrams of Fe-Ni alloys in water, which provides the first guide to its corrosion behavior based on the thermodynamic equilibrium, are presented. With the presence of chloride anions, localized corrosion, i.e. pitting corrosion, would take place through the breakdown of the passive layer formed on the surface. The mechanism of pitting corrosion and its influence by the effect of nickel content are the subjects of the following section.

2.4.1 Pourbaix Diagram of Fe-Ni Alloys in Water

Pourbaix diagram is developed based on the corrosion thermodynamic information, that is Nernst equation (for an electrochemical reaction involving electron transfer) or equilibrium constant (for chemical reaction), for a given metal on the equilibrium condition of pH value and potential with its environment, diagram of which is also referred to potential/pH diagram. Based on the Pourbaix diagrams [47] for Fe and Ni in Figure 2.10 (a) and (b) [48], thermodynamically stable phases can be identified, where solid lines represent the boundaries between the predominant chemical species. The superimposed dashed lines represent the stability limit of H_2O , as shown in Figure 2.10 (c)

[48], in which “line a” is for cathodic evolution of hydrogen and “line” b is for the anodic evolution of oxygen, and in the region between both lines indicate the stability of H₂O. The areas in Fe-H₂O diagram represents the stability species of iron on certain condition, where immunity means dissolution of iron (corrosion) would not take place thermodynamically, and passivity means a stable surface film is formed, such as oxide Fe₃O₄ and Fe₂O₃ based on the condition, which protects the iron surface. In the passivity region, corrosion may occur by diffusion of ions through oxide films, which is neglected in the diagram. By convention, the diagrams presented in this section represent a concentration of 10⁻⁶ M of the dissolved ions, which is the minimum concentration that corrosion is considered to occur. However, the Pourbaix diagram is limited to single elemental metals but not to alloys. For iron-nickel alloys, the material of this study, Fe-25Ni, the compound of NiFe₂O₄ [49] is not present in either diagram of iron or nickel. Therefore, the superimposition of both conventional diagrams leads to false information. The Fe-Ni composite with a molar proportion of Fe to Ni > 2 : 1 Pourbaix diagram at 298K (25 °C) is constructed by Thompson et al. [49], as presented in Figure 2.11 [49]. It can be noticed that nickel is relatively more noble than iron as the immunity area of nickel (Ni(s)) has partly overlapped with the stability area of water, indicating that the Ni(s) is the stable state and would not corrode in H₂O environment within that range of potentials and pH values in the overlapped region. Another limitation of Pourbaix diagrams is that the localized corrosion by chloride ions is not taken into consideration. The mechanism of localized corrosion-pitting, the focus of this study, will be presented in the following section.

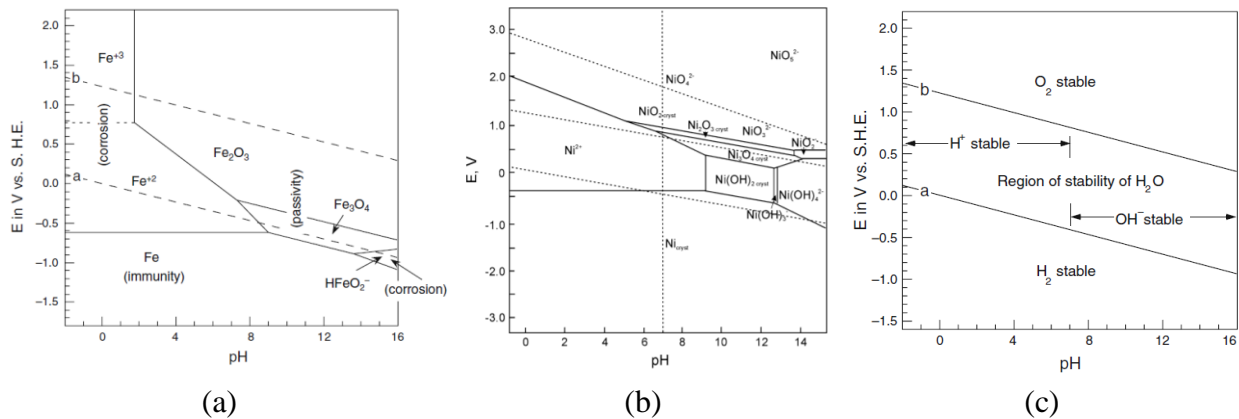


Figure 2.10 Pourbaix diagram for (a) iron, (b) nickel in water system and (c) water (at 25 °C; versus standard hydrogen electrode (SHE)) [48]

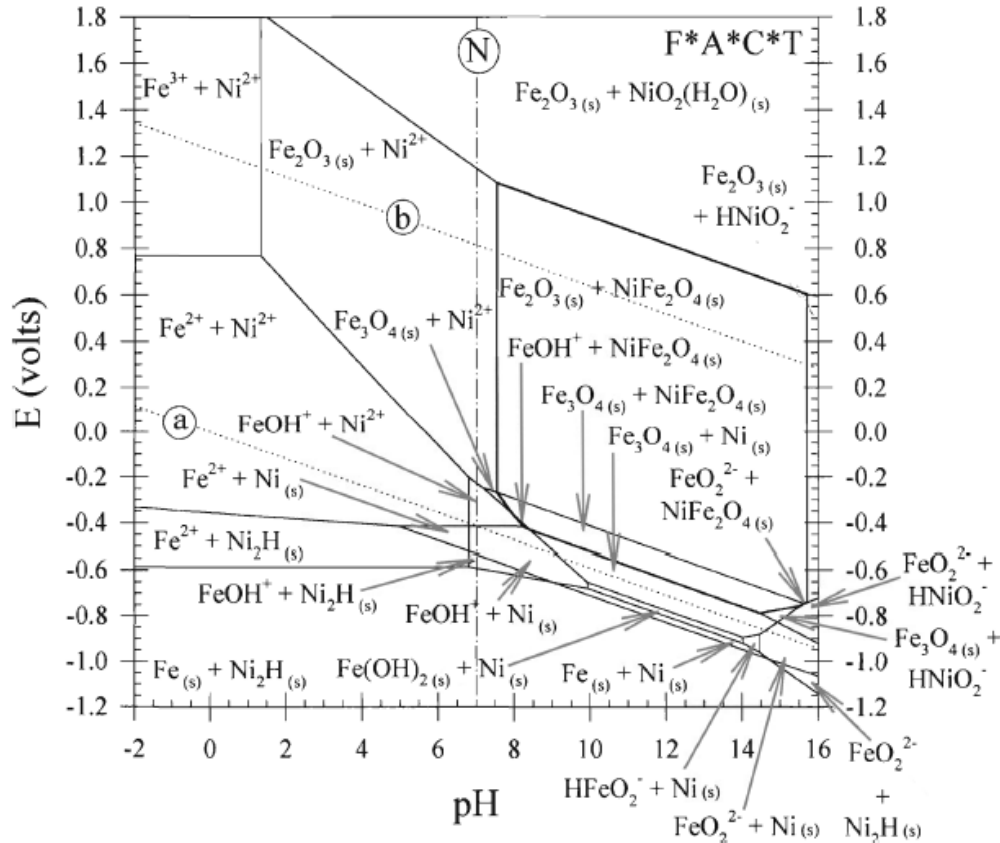


Figure 2.11 The Fe–Ni composite Pourbaix diagram at 298K in water system (at 25 °C; versus standard hydrogen electrode (SHE)) [49]

2.4.2 Localized Corrosion- Pitting

Localized corrosion, in contrast to general corrosion, occurs in passivating alloys that form protective oxide film, such as stainless steels, nickel alloys, aluminum alloys, when exposed to environments that contain aggressive ions such as chlorides (Cl⁻) [50]. Pitting refers to an extremely localized attack on the surface that produces destructive cavities or holes. To initiate pitting corrosion, the electrolyte acts as a strong oxidizer, while metal ions such as ferric act as electron acceptors and favor the formation of the passive film. Chloride ions then migrate from the electrolyte to the film interface and absorb on the outer surface of the passive film, permeate the metal oxide passive layer, and react with the underlying metal [51].

Pitting corrosion starts with the breakdown of the passive film, and the small unprotected area acts as anode and experiences anodic dissolution of the metal, while the rest of the metal surface remains passive and acts as the cathode. To maintain charge neutrality, excessive positive metal ions produced in the pits attract negative chlorine ions from the electrolyte, while the electrons released from the anodic dissolution transfer to the cathodic area. Localized mechanical damage to the protective oxide film such as a scratch or a dent, insufficient inhibitor coverage, and nonuniformities contribute to pitting corrosion.

The anodic reactions inside the pit are mainly the dissolution (oxidation) of iron:



The produced electrons travel through the solid metal to the surface, and participate in the cathodic reactions, as shown in Figure 2.12 [52]. The cathodic reaction can be expressed as:

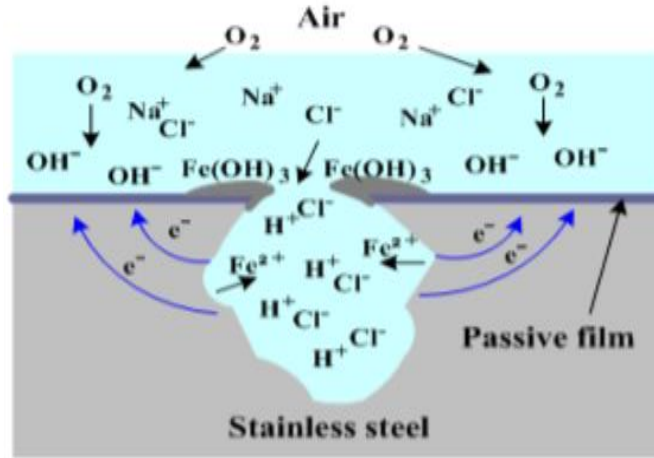
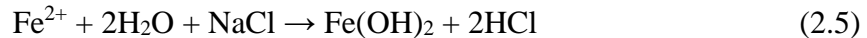


Figure 2.12 Generic schematic of pitting corrosion [52]

The Fe^{2+} ions generated inside the pit (equation 2.3) react with Cl^{-} ions that migrate into the pit for charge neutrality, and form FeCl_2 . The Fe^{2+} ions can also diffuse out of the pit and react with hydroxyl ion generated by the equation 2.4, and form $\text{Fe}(\text{OH})_2$ and $\text{Fe}(\text{OH})_3$ around the mouth of the pit. $\text{Fe}(\text{OH})_2$ can also form inside the pit through hydrolysis reaction [53]:



2.4.3 Effect of Nickel on Corrosion Behavior of Fe-Ni alloys

Iron-nickel alloys exhibit sensational corrosion resistance in an oxidizing environment, where the increased concentration of Ni in the alloy increases its corrosion resistance. Gehrman et al. [12] have conducted a humidity test on different iron-nickel alloys with nickel concentrations between 35 wt% and 82 wt% in between 25 °C and 80 °C, and found that with higher nickel contents the alloys experience less corrosion attacks. Wen et al. [54] have examined the influence of nickel on low alloy steels with 0.8, 2 and 5 wt.% Ni content in the mixed NaHSO_3 and NaCl solution at 25 °C by the technique of polarization curves, EIS and SEM. The corrosion current density decreased and the corrosion potential became more positive with the increment of nickel concentration. The charge transfer resistance of the low alloy steel increased with increasing nickel content, indicating that the corrosion dissolution reaction of the metal substrate was more difficult to carry out, which was mainly due to the formation of the passive protective layer; Its resistance also increased with

the increasing nickel concentration, showing that the corrosion resistance of the passive layer was higher and acted as a barrier to prevent further corrosion.

The SEM results revealed that the structure of the passive layer of the nickel-containing steel consisted of double layers, an adherent and compact inner rust layer which reduced the active area for corrosion and prevented the penetration of corrosion ions, such as chloride, and an outer layer with less adherent and more porous structure, while the carbon steel composed of only one single rust layer with relatively high porosity. The compactness and adhesion of the inner passive layers improved with the increase of nickel content. However, no details of the chemical composition of the two layers were provided in Wen's study [54]. The double-layer structure of Fe-Ni alloys formed in a Cl-rich environment is consistent with the results found by Konishi et al. [55], who further analyzed the composition of the inner layer of Fe-Ni alloys. The results indicated that the layer consisted mostly of akaganéite (β -FeOOH) with a molar ratio higher than 60%, and its molar ratio increased with increasing nickel content.

The thicker and more protective passive layer resulting from higher Ni content improved the general corrosion behavior as well as the localized corrosion resistance of Fe-Ni alloys. The cyclic potentiodynamic polarization (CPP) technique was conducted on Fe-36%Ni and Fe-45%Ni alloys in 1M HCl solution by Alharthi et al. [55]. For general corrosion, the E_{Corr} was less negative and J_{Corr} was lower for higher-Ni-content alloy, which was consistent with the results by Wen [54]. Upon reversing the applied potential in the backward direction, the obtained current value increased in comparison with the current density in the forward scan at the same potential, exhibiting positive hysteresis, which was related to the decreased degree of passivity due to localized corrosion, pitting corrosion in this case, indicating the difficulty in surface repassivation or stopping the propagation of pits [56]. The values of current and the hysteresis loop obtained for Fe-36%Ni alloy were much higher than Fe-45%Ni alloy, which was an indication of higher intensity of pitting corrosion. The open-circuit potential (OCP) for both alloys shifted to a more noble direction with increasing immersion time, which was resulted from the formation of corrosion product (rust layer) that hindered the corrosion attack by blocking the surface area of the alloys, and Fe-45%Ni alloy exhibited less negative value due to the formation of a thicker rust layer, which was confirmed by SEM micrograph.

2.4.4 Effect of Phases on Corrosion Behavior of Steels

The effect of nickel, which is a γ -stabilizer element, was reported to increase the fraction of austenite phase in the matrix during laser treatment with increasing nickel content [57], resulting in an improved corrosion behavior as the corrosion rate (current density) decreased due to its better corrosion resistance. The retained austenite also improved the local corrosion resistance, as discussed in section 2.2.2. However, the galvanic effect could take place between different phases due to corrosion potential gradients [13]. Conventionally, the difference in potentials can be a result of compositional change, which includes element depletion caused by carbide precipitation at grain boundaries [19] and differences in passivating element content between phases [58]. Microstructural change has also been reported to contribute to galvanic corrosion, such as strained-

induced martensite and deformation bands in the austenite matrix [13]. The structural change led to a reduction in corrosion potentials, indicating strained-induced martensite is electrochemically more active than the austenitic matrix, which can cause micro-scale galvanic corrosion that deteriorates the corrosion resistance. As a result, the change in corrosion behavior is the trade-off between the beneficial effect of austenite phase in the matrix and the detrimental effect of galvanic corrosion due to compositional and microstructural change.

3. Materials and Methodology

In this chapter, the materials and methodology used in this work are listed. The microstructures are characterized by optical and scanning electron microscopy equipped with an energy dispersive X-ray spectroscope (EDS); The corrosion behavior is analyzed by open-circuit potential measurement followed by potentiodynamic polarization tests.

3.1 Material and Initial Heat Treatment

The composition of the investigated material is listed in Table 3.1. The alloy was vacuum cast in an 80mm x 80mm x 400mm billet that was subsequently forged to a 50 mm x 50 mm x 1000 mm billet and homogenized at 1273 K for 12 hours. Flat coupons of 1 mm were machined from the billet with the use of an Electrical Discharge Machine (EDM). In this research, the dimension of the specimens is 110 mm in length, 20 mm in width and 1mm in thickness.

	Fe	Ni	C	Mn	Si	Mo	Al	S	P	Cr
wt-%	Balanced	24.90	0.20	0.02	<0.01	<0.01	0.005	0.002	0.003	0.02

Table 3.1 Alloy composition

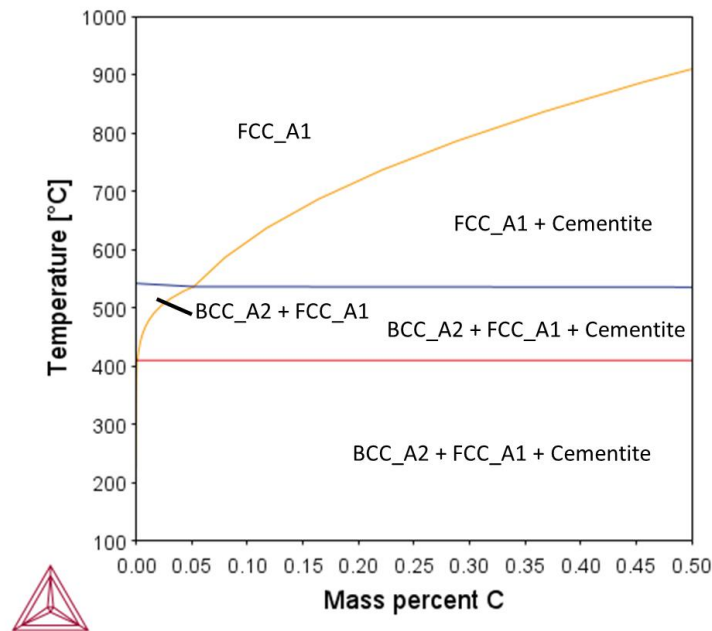


Figure 3.1 Equilibrium phase diagram of Fe-25Ni with different carbon content [59]

As displayed in Figure 3.1 [59], the equilibrium phase diagram of Fe-25Ni with different carbon concentrations is calculated by ThermoCalc software [59], and at room temperature, the phase consists of a mixed structure of FCC_A1 (austenite), BCC_A2 (ferrite) and cementite. The non-equilibrium parameter, M_s , was calculated to be 291K using JMatPro 4.0. [61]

Initially, the alloy was immersed in an alkali chloride salt bath at 1173K for 60 seconds for full austenitization, followed by water quenching to obtain an austenitic microstructure. In order to completely transform the austenite, the samples must be cooled down to or below its martensite finish temperature, M_f , indicating the necessity of performing a cryogenic treatment. The alloy was further immersed in liquid nitrogen (LN_2 , temperature: 77K) for 600 seconds for the martensitic transformation. Furthermore, the martensitic alloy was tempered at 523K for 1800 seconds and air-cooled to room temperature. After the treatment, three different specimens are obtained: austenite, as-quenched martensite and tempered martensite specimens.

3.2 Laser Heat Treatment

After the initial heat treatment, a continuous wave Trumpf Trudisk 8002 Nd:YAG laser with a wavelength of 1064 nm was utilized for localized single-tracked laser treatment. The surface of the specimens remained unground for the avoidance of the reflection of the laser radiation. In order to investigate the effect of laser parameters on the microstructure and the laser affected zone, the laser power (P) and the laser scanning rate (v) were varied. The divergence angle of this laser is around 16 degrees. When the laser height is 60.5mm, the laser spot is at its minimum $d \approx 0.2$ mm. By increasing the height, the spot size also increases. The distance between the laser optics and the workpiece (h ; laser height) was adjusted to 185mm to maintain the laser spot size ≈ 0.8 mm, and the parameter setting is listed in Table 3.2. To assess the combined effect of laser power and scanning speed, linear laser energy density E_L (unit: J/mm) is used [62]:

$$E_L = P/v \quad (3.1)$$

The beam spot size is defined assuming a Gaussian beam profile as it dropped to $1/e^2$ of its intensity. In this research, the parameters of laser line 8 are applied on both as-quenched martensite and tempered martensite specimens to investigate the effect of localized laser treatment on corrosion behavior. The corresponding microstructure of the surface and cross-section is shown in Figure 3.2. There are 3 distinct zones: melt, laser-affected zone (LAZ), and bulk martensite. The melt is not present in the top-surfaced image due to grinding and polishing.

Argon was used as the shielding gas in this experiment, which serves to suppress laser-induced plasma and vapor. During the interaction between the laser beam and plasma or vapor, the laser energy is attenuated due to the absorption and refraction of laser-induced plasma to the laser beam, and leads to the prevention of the full power density in the incident laser beam from reaching the workpiece [63]. Using a shielding gas is considered as an effective method to suppress the laser-induced plasma, and helium is also widely used as shielding gas due to its good thermal conductivity and high ionization energy.

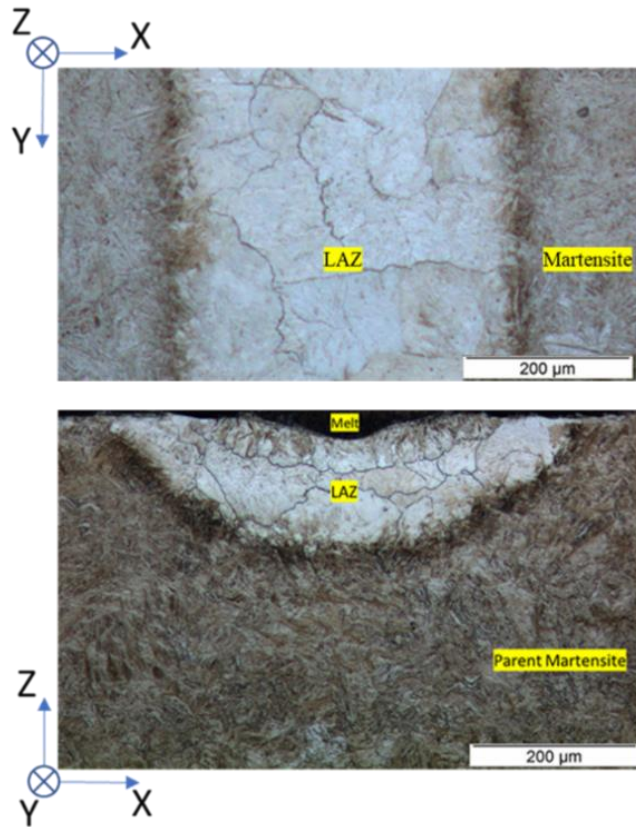


Figure 3.2 Optical images of the top surface (upper) and cross-section (lower) of laser line 8 on as-quenched martensite

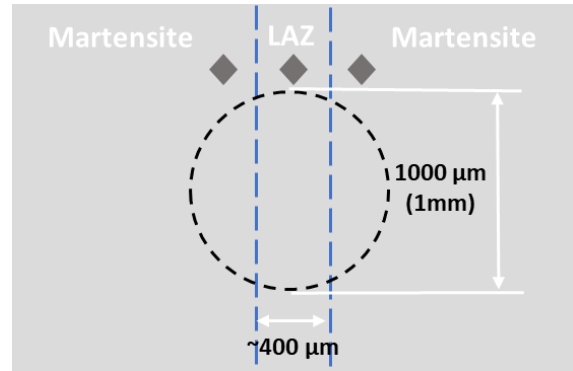


Figure 3.3 Schematic of tested surface of lasered specimens in corrosion analysis (Dark grey triangles: indentation of hardness test for positioning the LAZ)

Line	1	2	3	4	5	6	7	8
P(W)	400	400	200	200	160	160	160	160
v(mm/s)	25	50	25	50	50	120	150	200
E _L (J/mm)	16	8	8	4	3.2	1.33	1.06	0.8

Table 3.2 Laser parameters setting

The specimens were denoted as LSR-M and LSR-TM for M and TM after the laser treatment, respectively. (The limitation of the laser: minimum 160W of the laser power (P) and maximum 208 mm/s of the scanning rate (v))

3.3 Sample Preparation

To maintain the consistency of the surface quality, all the samples were ground on a Struers rotary grinder with grid grinding papers of P800, P1200, and P2000 sequentially, and polished to 1-micron polishing paste. In the end, the surface was cleaned with isopropanol and properly dried.

3.4 Microstructure Characterization

In order to reveal the grain boundary of austenitic microstructure, the sample was first ground and polished as mentioned in the sample preparation section, and etched with waterless Kalling's #2 etchant (composition: 5 grams of CuCl_2 + 100 ml of Hydrochloric acid+ 100 ml Ethanol). For the reveal of martensitic microstructure, Nital 2% etchant (2 ml of nitric acid + 100 ml of ethanol) was used.

For the examination of the microstructure and the three-dimensional depth measurement, light optical microscopy was performed using a Leica DMLM optical microscope and a Keyence VHX-100 Digital microscope. For a detailed characterization of the microstructures, the morphological images and the compositions of the specimens were obtained by utilizing a JEOL JSM-IT100 scanning electron microscope (SEM; in secondary imaging detection mode) equipped with an energy dispersive X-ray spectroscope (EDS).

3.5 Corrosion Analysis

After the surface is well polished to achieve the condition for the following corrosion tests, the laser affected zone (LAZ) is not distinguishable. To precisely locate the position of the laser affected zone (LAZ), micro-indentation was conducted on both LSRM and LSRTM by an EMCO G5 DuraScan, with a distance of 500 microns between the indentations. The corrosion behavior of the specimens A, M, TM, LSRM, and LSRTM was investigated in a 3.5 wt% NaCl solution at room temperature by open-circuit potentials (OCP) and potentiodynamic polarization measurements. The duration of the OCP experiments is 90 minutes for A, M, and LSRM, and 10 minutes for TM and LSRTM. The potentiodynamic polarization experiments were performed by scanning the potential from -0.25 V (versus OCP) in the positive direction to $+0.25$ V (versus OCP) for non-lasered specimens, and -0.5 V (versus OCP) in the positive direction to $+0.5$ V (versus OCP) for lasered specimens. The scan rate was set to be at a value of 0.167 mV/s. All the corrosion tests were conducted by BioLogic Potentiostat, with a stainless steel mesh used as a counter electrode and an Ag/AgCl, KCl(saturated) electrode used as a reference electrode, and the data was acquired by the software EC-Lab.

The exposed area of the working electrode was 28.28 mm² (diameter: 6 mm) for non-lasered specimens (A, M, and TM) and 0.79 mm² (diameter: 1 mm) for lasered specimens (LSRM and LSRTM). The 1-mm-diameter exposed area includes the LAZ with a width of roughly 400 μm and the base as-quenched martensite, and the coverage percentage of the LAZ area is around 53%, as shown in Figure 3.3.

4. Results and Discussion

In this chapter, the bulk microstructure of Fe-25Ni-0.2C formed by initial heat treatment is presented firstly, which is characterized by optical microscopy and scanning electron microscope (SEM). Following that, the effect of laser with different processing parameters, including laser power (P) and scanning speed (v), on the microstructure is discussed.

For the corrosion analysis, the results of open circuit potential (OCP) measurement of different specimens-austenite, martensite, tempered martensite, lasered martensite and lasered tempered martensite, are presented, which is followed by the results of potentiodynamic polarization curves. The effect of initial and laser heat treatment on corrosion behavior is discussed in detail. Next, surface morphology after the corrosion test is examined by optical microscope to evaluate their pitting corrosion behavior. In the end, the corrosion product and pits are further characterized by SEM and EDS analysis.

4.1 Effect of Heat Treatment on Microstructure

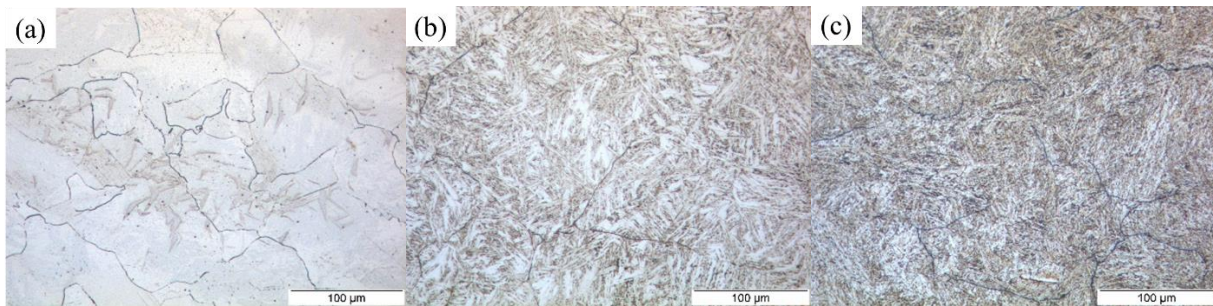


Figure 4.1 Optical microscopy images of (a) austenite, (b) martensite and (c) tempered martensite specimens

The base austenitic microstructure is shown in Figure 4.1 (a). With the application of the intercept method by ImageJ software [64], the average austenite grain size is $67 \pm 5 \mu\text{m}$ was obtained. It is observable that a large population of butterfly martensite is formed on the surface, which corresponds to a 0.25 ± 0.01 weight fraction of the martensite phase in the XRD result. The microstructure of cryogenically formed martensite is shown in Figure 4.1 (b). The white-etched butterfly wings consist of a single twin pair of martensite with a relative misorientation angle of 16° [45, 65]. XRD analysis revealed a 0.08 ± 0.01 weight fraction of the austenite phase in this microstructure. After tempering heat treatment in an oven at 523K for 1800 seconds and air-cooled to room temperature, the microstructure of tempered martensite is revealed in Figure 4.1 (c). The white-etched butterfly wings are not clearly distinguishable compared to the as-quenched specimen, and the entire microstructure turns slightly brownish which is likely due to the precipitation of carbides. A more detailed microstructural analysis is shown in Figure 4.2. The most pronounced difference between the SEM images is the presence of a high population of very fine, nanoscale needle-type carbides that precipitate within the butterfly wings in the tempered specimen.

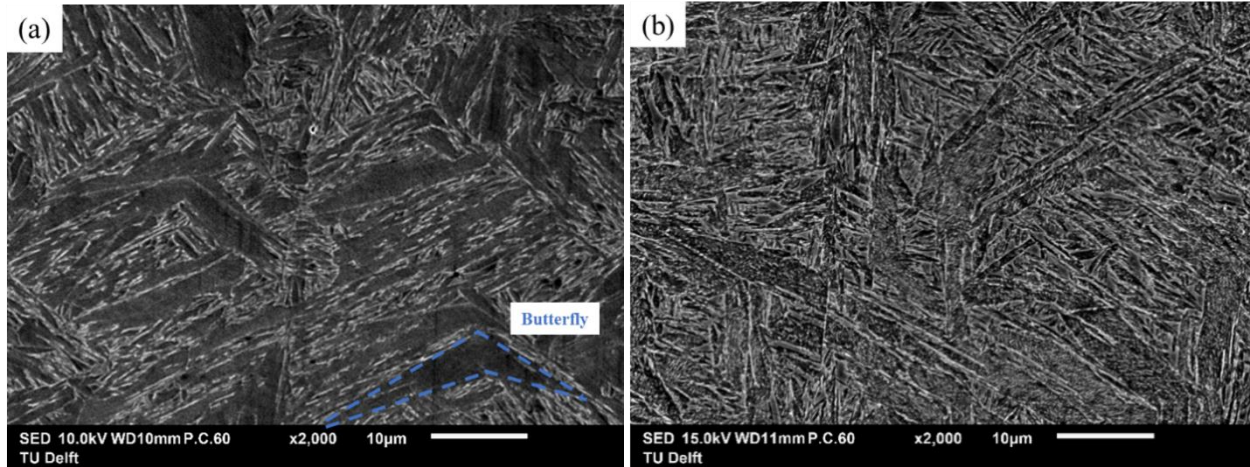


Figure 4.2 SEM images of (a) as-quenched martensite (b) tempered martensite

4.2 Effect of Laser Parameters on LAZ and transformation mechanisms

In Figure 4.3, with microstructural analysis, the optical microscopy images show different well-distinguished zones in the cross-section image of LSRM-line 8 ($P=160\text{ W}$, $v=200\text{ mms}^{-1}$): the melt, laser affected zone, interface, and the bulk martensite phase. The depth of the melt is around $30\text{ }\mu\text{m}$. In the laser affected zone, where only solid-state transformation occurs, the martensite phase was reverted to austenite during the laser process, which can be further distinguished as fine-grained and coarse-grained austenite. In this region, the grain boundaries of austenite were revealed after etching with waterless Kalling. The austenitic microstructure is relatively dark-etched in the fine-grained region compared to the coarse-grained region. The layer of fine-grained austenite is up to a maximum of $70\text{ }\mu\text{m}$ in depth in the middle which decreases when moving away from the center, indicating a Gaussian beam profile that has the highest intensity of laser at the center, and the thickness of the coarse-grained austenite layer is $100\text{ }\mu\text{m}$. The overall depth of LAZ is $170\text{ }\mu\text{m}$. The interface between the austenite and martensite is distinguished by dark etching, which corresponds to a temperature range of the austenite start temperature (A_s) to the austenite finish temperature (A_F).

In this work, the effect of laser power and laser scanning speed on the microstructure is investigated. As displayed in Figure 4.4. For laser line 1 to line 4, the specimens were etched with Nital 2%. The microstructure revealed is very different from laser lines 5 to 8, which were etched with non-aqueous Kalling solution. The interface of LAZ and martensite etches darkly, but the grain boundaries of austenite are not clearly visible. From comparing lines 3 and 4, it is observed that with an increase of scanning speed from 25 to 50 mms^{-1} , the linear laser energy density has decreased from 8 to 4 Jmm^{-1} , which leads to a microstructural change from full-penetration (exceeding the thickness of the specimen: 1 mm) LAZ to the formation of LAZ with the depth of approximately $430\text{ }\mu\text{m}$. The same effect is observed for laser lines 5 to 8, the depth of LAZ decreases from around $420\text{ }\mu\text{m}$ to $170\text{ }\mu\text{m}$ as the laser power is fixed at 160 W . Reduced laser power also causes a decrease in the laser energy density, and hence the depth of LAZ, which can be

observed between line 2 and 4 as the laser power drops from 400 W to 200 W. All the specimens show evident signs of melting. The width of LAZ is also influenced by the laser power and laser scanning speed, and it decreases as the corresponding laser energy density reduces. The width of LAZ for laser line 8 is around 595 μm . It is worth noting that linear laser power density is just a gross simplification. Laser line 2 ($P=400\text{ W}$, $v=50\text{ mms}^{-1}$) and line 3 ($P=200\text{ W}$, $v=25\text{ mms}^{-1}$) both correspond to 8 Jmm^{-1} , but exhibit slightly different microstructure as the LAZ shows deeper penetration for the latter, as shown in Figure 4.4 (b) and (c).

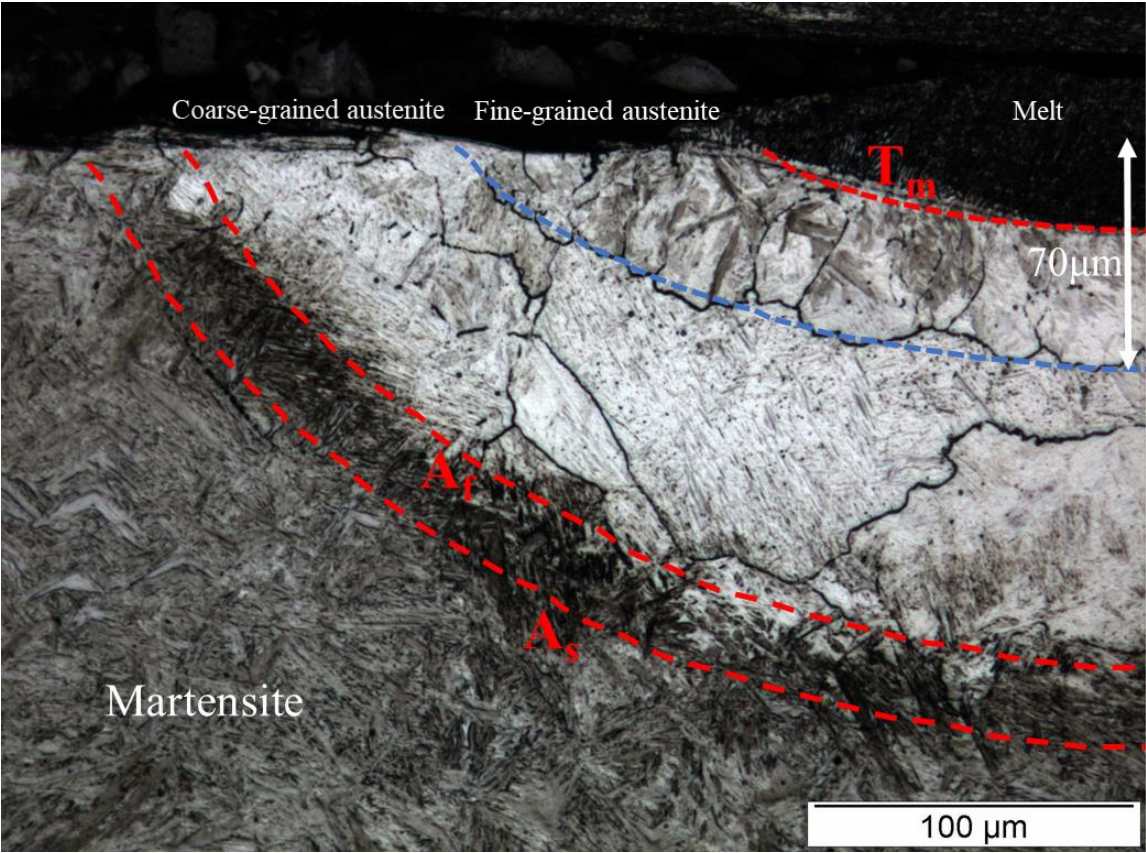


Figure 4.3 The optical images of cross-sectioned LSRM-line 8 showing different zones of melt, LAZ and parent martensite

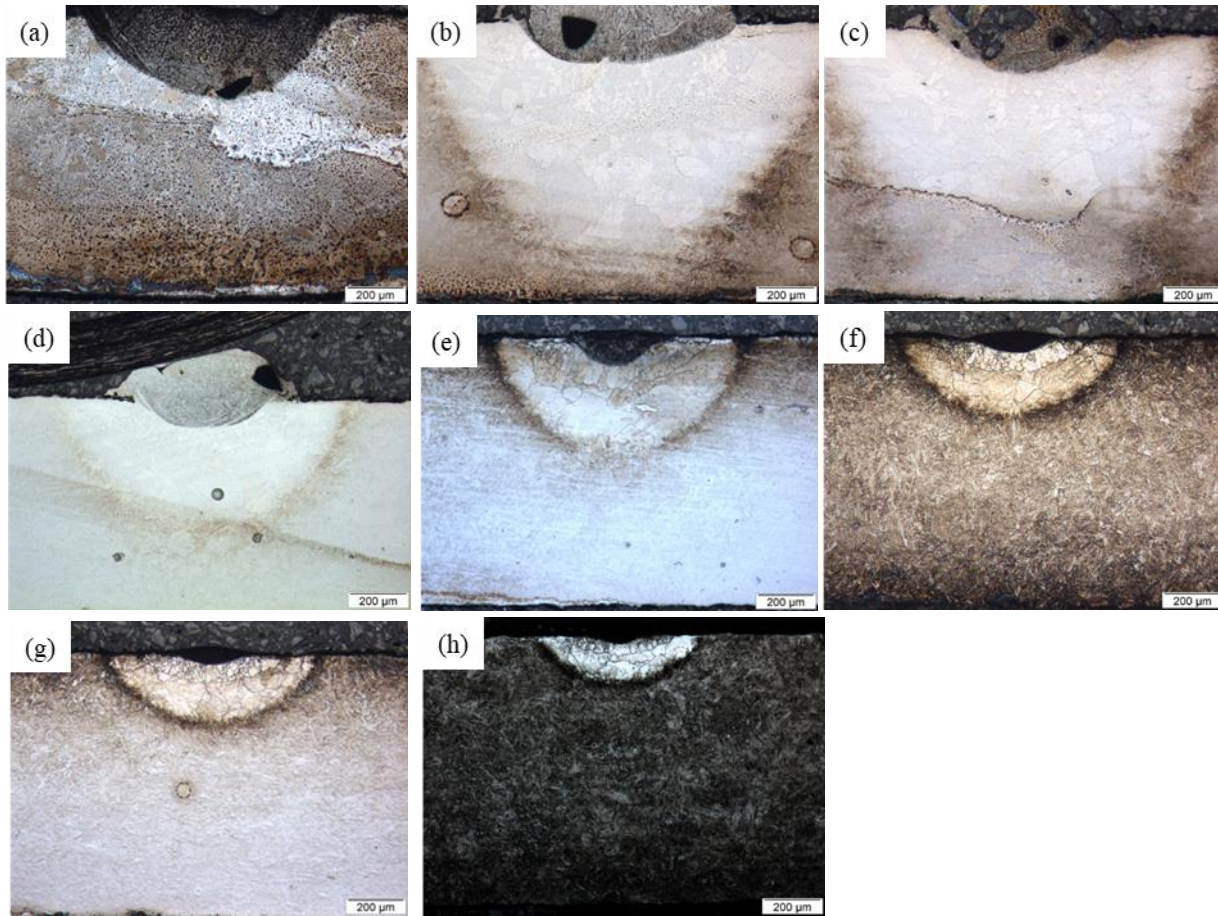


Figure 4.4 Optical microscopy images of laser lines 1 to 8 on as-quenched martensite, which corresponds to (A) to (H), respectively (Etchant: line 1-4: Nital 2%; line 5-8: waterless Kalling)

According to the as-mentioned heat equation by D.R. Poirier et al. [29], the heat generated by laser at laser focal spot spreads evenly in all directions in an isotropic solid, which results in a rapid change in temperature at a point where large spatial gradient of thermal exist, and the temperature change rate decreases as the distance from the laser spot increases [30]. Therefore, different transformations take place at different zones. These zones can be distinguished as (i) melt region, (ii) laser affected zone (LAZ) and (iii) as-quenched martensite region, respectively, from the position closed to the laser spot to far away from it, as seen in Figure 4.3 for the lasered martensite-line 8 specimen. The lasered tempered martensite specimen has a similar dimension of LAZ, but some differences in the microstructure can be expected. The rapid heating during laser surface treatment would suppress the diffusion process, which leads to the formation of a LAZ with more undissolved carbides and precipitates. In this section, only the lasered martensite specimen is investigated.

(i) Melt region:

The surface of the material is heated by the laser radiation to its melting point. Figure 4.5 shows the microstructural characteristics of laser line 8 ($P=160W$, $v=200\text{mm s}^{-1}$): in the melt region, where

very fine grains with dendritic structure can be found, the microstructure of which is comparable to the finding of selective laser melting (SLM) of Fe-30%Ni alloy by Zhang et al.[66]. The condition for dendritic fine grains to form is the molten material (liquid) to be undercooled, or supercooled, below the freezing point of the solid prior to solidification [67]. For laser application, it can be attributed to the intense heat absorption from the laser source and elimination of heat between molten pool and substrate. Moreover, the Marangoni flow (thermocapillary flow) in the molten pool, which is a result of the thermal gradient, can lead to a high nucleation rate during solidification. Rapid cooling with a large undercooling lead to an increase of nuclei and hence small dendrite grain size. In this case, micron-scaled dendritic fine grains are formed in the melting area.

In this region, the transport of heat is governed by two forms: conduction and convection. Marangoni flow, which has a dominant influence on mass and heat transfer within the molten pool [68, 69, 70], is caused by surface tension gradients ($\frac{d\gamma}{dT}$), and it determines the dimension and geometry of the melt pool. For pure and most alloys [62] with low content of surface-active elements, such as sulfur [71], the melt flow is radially outward (from the center to the edge of the melt) due to their negative surface tension gradients ($\frac{d\gamma}{dT} < 0$, the surface tension (γ) reduces with an increasing temperature), resulting in the formation of the shallow/broad instead of the deep/narrow melt pool, same as the geometry of the melt in this study.

The effect of the laser parameters on the characteristics of the melt pool can be compared. The dimension of the melt decreased when there was a decrease of 400 W to 200 W in laser power, as in Figure 4.4 (b) and (d), the width reduced from around 750 to 550 μm , and the depth reduced from around 155 to 100 μm , which results from lower peak temperature obtained by lower laser power input. As scanning speed increases, the laser–powder interaction time is less to absorb energy, both the width and the depth reduced from around 415 to 280 μm and 100 to 30 μm , respectively, as shown in Figure 4.4 (e) to (h). The unevenness of the melt at the surface can be observed, which is a result of surface tension at the air-liquid interface [72].

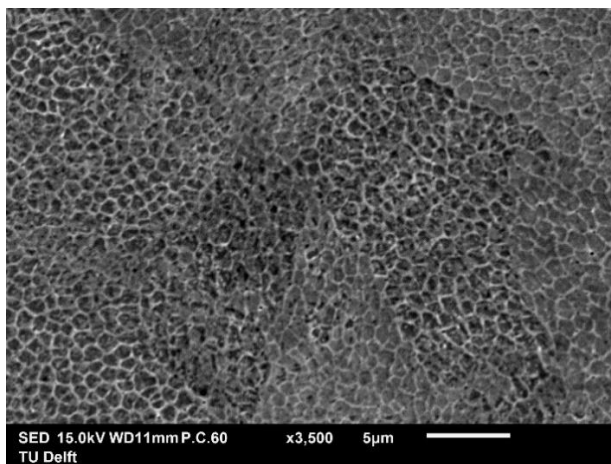


Figure 4.5 SEM micrographs of the melting zone of LSRM-line 8

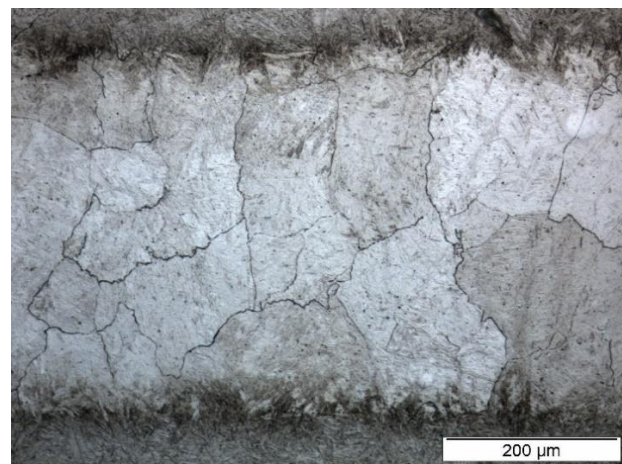


Figure 4.6 Optical microscope images of laser affected zone (etched with waterless Kalling)

(ii) Laser affected zone (LAZ):

After laser treatment (line 8: $P=160\text{ W}$, $v=200\text{mm s}^{-1}$) on as-quenched martensite, the specimen surface is ground and polished until the melt zone is removed, and the OM images of the laser affected zone are shown in Figure 4.6. Comparing it with its cross-sectioned microstructure in Figure 4.3, the melting zone and fine-grained austenite, which is up to around $70\text{ }\mu\text{m}$ in depth from the surface, are removed due to sample preparation. As a result, the microstructure corresponds to the region of coarse-grained austenite, where the average grain size is measured to be $102 \pm 5\text{ }\mu\text{m}$. In this study, the following corrosion test is conducted based on this microstructure of coarse-grained austenite and bulk martensite.

Large austenite grains are formed in the LAZ close to the reverted austenite/martensite interface. The grain structure appears to be relatively curved or wavy rather than straight, as seen in Figure 4.7, which is a result of the displacive (martensitic) transformation observed by Krauss [73]. Although displacive transformation is often applied for grain refinement [74], the phenomenon of so-called austenite memory is also reported, which under certain conditions, the reverted austenite is found to be similar to that of prior austenite in terms of grain boundaries, shape, size and orientation. The same effect is also reported by Alaei et al. [75] when conducting cyclic reverse martensite transformation on Fe-24Ni-0.3C alloys that has a similar composition to the material of this study.

Fine-grained austenite is formed at the near-surface region bordering with the melting zone, where the heating rate and temperature achieved during the laser process is relatively high, and is most likely through the mechanism of recrystallization. Recrystallization is driven by the stored energy of deformation, since the reverted austenite through martensitic (displacive) austenite transformation is high in dislocation density, as reported by Shirazia et al. [76] for Fe-23wt%Ni alloys, due to the inheritance of high density of dislocation in initial martensite into the austenite [77] and the newly generated dislocation. As a result of recrystallization, the newly formed austenite grains, which have different grain orientations and shapes, show relatively straight grain boundaries [78], as shown in Figure 4.7.

(iii) As-quenched martensite:

In the region far away from the LAZ, the base material has not been affected by the heat generated by the laser source. The morphology of the martensite is determined by its accommodation process for the transformation strain, which is dependent on its formation temperature [44]. The butterfly-type martensite in this region, as marked with a dashed line in Figure 4.2 (a), has a relatively high formation temperature [43] compared to lenticular and plate-like martensite, accommodation of which occurs by twinning and dislocation slip on limited slip systems [44]. In the region near the LAZ, the tempering of martensite by the laser heat can be expected, which leads to different mechanical properties, such as lower hardness, than the as-quenched martensite far away from the LAZ.

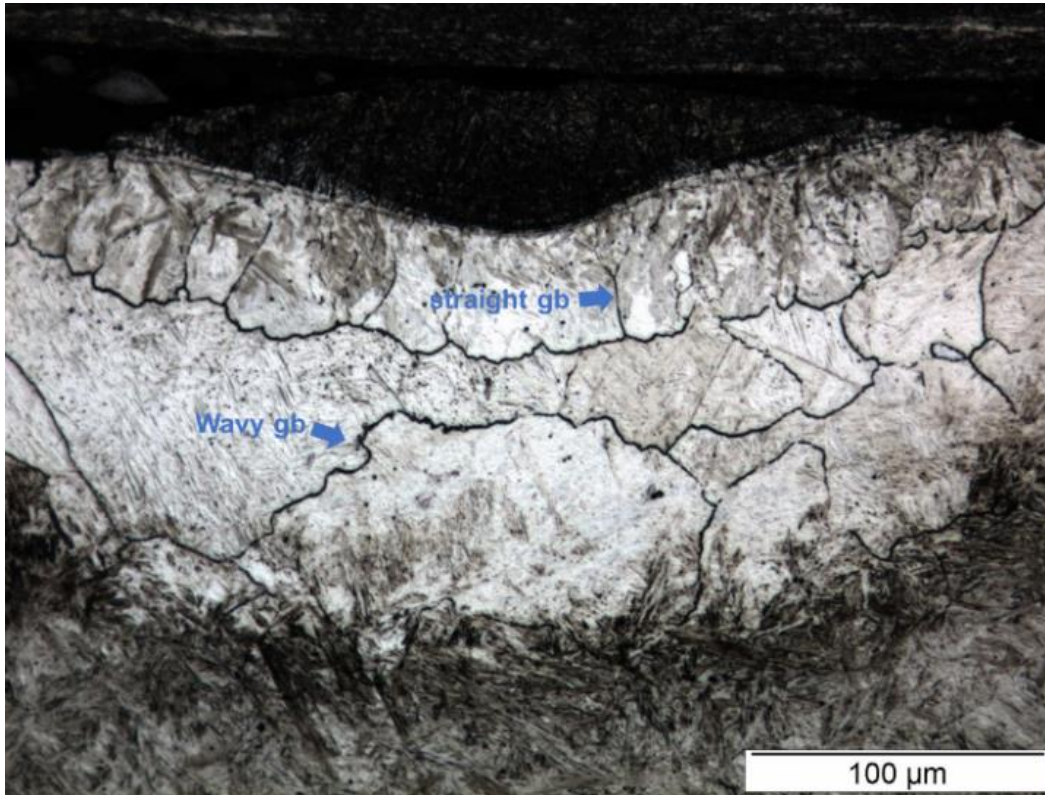


Figure 4.7 Grain structure in LAZ (fine-grained austenite: straight grain boundary; coarse-grained austenite: wavy grain boundary)

4.3 Corrosion Behavior of Fe-25Ni-0.2C

4.3.1 Open-Circuit Potential (OCP) Analysis

The open-circuit potential (OCP) curves of different Fe-25Ni-0.2C specimens in 3.5% NaCl solution are depicted in Figure 4.8. All the specimens have been repeated once to obtain the averaged data. The initial potential of austenite was measured to be -0.152 V versus Ag/AgCl electrode, and it shifted in the less negative direction with increasing immersion time. There were slight voltage drops of less than 10 mV from 2000 to 4000 s. At the end of the run (after 5400 seconds), the potential was $-0.092 \text{ V}_{\text{Ag/AgCl}}$, and the fluctuation of OCP was 3.1 mV over the last 600 seconds, indicating that the system was relatively stable. The value of OCP for as-quenched martensite shifted in the more noble direction from the initial potential of $-0.138 \text{ V}_{\text{Ag/AgCl}}$, but slightly dropped by less than 7 mV from 3500 seconds to the end. It recorded $-0.117 \text{ V}_{\text{Ag/AgCl}}$ at the end of the measurement. The trend of potential shift to the less negative direction can be related to the thin protective layer of corrosion products formed during the immersion, which hindered the corrosion attack to the surface by covering its exposed area [55].

The OCP curves of tempered martensite specimens were presented. It is worth mentioning that both tests showed large variation with several potential drops of 20 mV to over 100 mV, and the curves fluctuated throughout the entire period. The fluctuated curves indicate that the tempered

specimens might be highly reactive in the environment of 3.5% NaCl solution, and hence the unstable behavior. As a result, the time period for OCP measurement for tempered martensite was then reduced to 600 seconds. The potential at the end of the run was $-0.105 V_{Ag/AgCl}$.

The results of lasered specimen, LSRM and LSRTM, with the parameters of laser line 8 ($P=160 W$, $v=200 \text{ mms}^{-1}$) were displayed in Figure 4.8. The OCP curves of LSRM showed similar trend as the recorded potential shifted to less negative direction with increasing time, and the curves stabilized at the end of the run, recording potential of $-0.123 V_{Ag/AgCl}$. For the lasered tempered martensite, a few sudden drops of potential could be observed, indicating its relatively unstable characteristic. For the consistency, the averaged data presented in Table 4.1 is based the OCP value recorded at 600th second. Both martensite and tempered martensite recorded much lower OCP after the laser treatment.

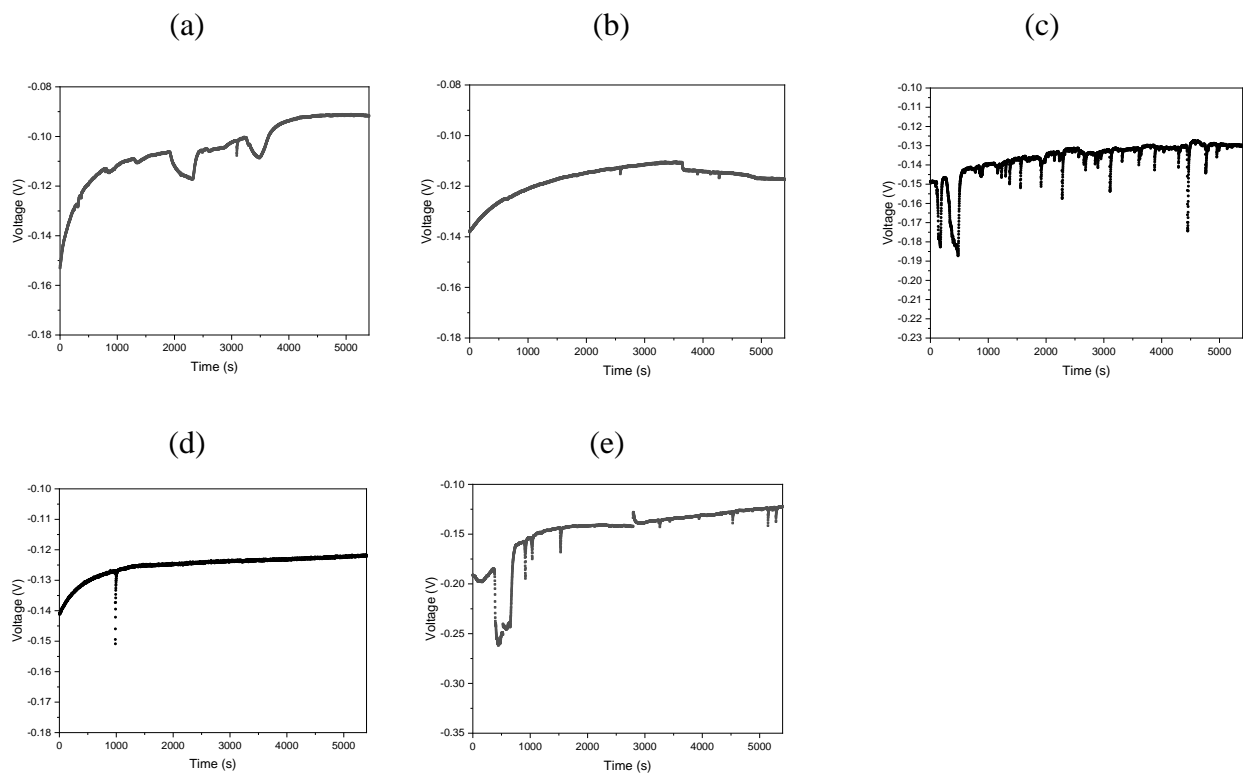


Figure 4.8 Open-circuit potential (OCP versus Ag/AgCl) of (a) austenite, (b) martensite, (c) tempered martensite, (d) lasered martensite, and (e) lasered tempered martensite with time in 3.5 % NaCl solution

	Austenite	Martensite	Tempered Martensite	Lasered Martensite	Lasered Tempered Martensite
OCP ($V_{Ag/AgCl}$)	-0.136 ± 0.028	-0.146 ± 0.020	-0.139 ± 0.026	-0.142 ± 0.012	-0.253 ± 0.102

Table 4.1 The mean OCP for each specimen in 3.5 % NaCl solution at 600th second

4.3.2 Potentiodynamic Polarization Curves

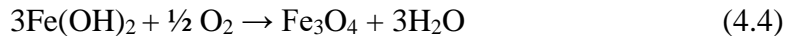
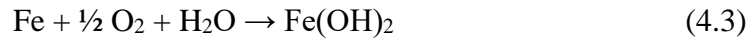
Following the OCP measurement, the pitting corrosion behavior of the specimens in 3.5% NaCl solution was investigated by Tafel extrapolation of potentiodynamic polarization curves. The polarization curves, which were obtained with a potential scan of ± 250 mV about E_{ocp} for austenite, as-quenched martensite, and tempered martensite. In cathodic branch, the decrease of the cathodic current density with increasing applied potential till reaching the values of the corrosion currents is due to the reduction of oxygen on the surface of the alloy (in neutral and alkaline solutions), which is described as follows:



In the anodic branch, the dissolution reaction of the material takes place at the surface, resulting in an abrupt increase of current density with the increasing applied potential. With further potential scan in anodic direction, the current density increases slowly due to the formation of a corrosion product layer on the metal surface to prevent the continual dissolution, which is also referred to “passivation”. Based on the finding from Condit [79], who analyzed the anodic potentiodynamic polarization behavior of Fe-Ni binary alloys with different weight percentages of iron, and the finding showed that the dissolution reaction in the active region is controlled by iron if the weight percentage of iron is above the critical value of 48.8 wt. % (50 at. %). Therefore, the increase of anodic currents with potential in the active region is contributed by the dissolution of metallic iron from the alloy to ferrous cations Fe^{2+} , reaction of which is expressed as follows [80]:



With further increase in the potential, an oxide layer is formed to protect the surface from dissolution, and hence the slow increase in current density with the increase in potentials in the anodic direction. The layer is formed through the reaction [80]:



The trend of passivation and corresponding slow increase in current density was discovered by Sherif [80], who conducted corrosion analysis on Fe64/Ni36 and Fe55/Ni45 in 4.0% NaCl.

In the presence of chloride ions, the current density rises drastically as the potentials increases beyond the critical pitting potential, which is defined as the potential at which the passivation breaks down locally, leading to the initiation of pitting. Therefore, pitting potential (E_{pitt}) could be used as an index of resistance to localized corrosion. The corrosion parameters, such a corrosion potential (E_{corr} , potential at which the rate of anodic dissolution equals the rate of cathodic reduction), corrosion current density (i_{corr} , dissolution current density at the corrosion potential), pitting potential (E_{pit}), and passivation interval ($E_{pit} - E_{corr}$, as an index of stability of passive film) were obtained from the polarization curves, which were presented on Figure 4.9. It is worth mentioning that austenite in Figure 4.9 (A, black curve) showed signs of metastable pits at around

-1.02 V_{Ag/AgCl} in the passive region, which caused an increase in recorded anodic current density. Same trend could be observed for tempered specimen Figure 4.9 (TM, blue curve), metastable pits nucleated and grew but they were repassivated quickly after the growth, causing some fluctuations in the anodic curves below the critical pitting potential. For each specimen, the averaged corrosion data (\pm standard deviation) is presented in Table 4.2. Austenite exhibits slightly better pitting corrosion resistance with a higher pitting potential of 0.074 V_{Ag/AgCl} and passivation interval of 0.275 V_{Ag/AgCl} compared to martensite. The tempering treatment has a detrimental effect on pitting corrosion behavior by shifting the pitting potential to a more negative direction and reducing the passivation interval.

Comparing between the specimens prior to laser treatment, austenite specimen has exhibited the best resistance to localized corrosion among all three by recording the highest E_{pit} of 0.074 V_{Ag/AgCl} and E_{pit}-E_{corr} (passivation interval) of 0.275 V_{Ag/AgCl}, while tempered martensite specimen is the most susceptible to pitting with pitting potential recorded in a more active direction. However, it should be clarified that this does not serve as a direct indication of the corrosion behavior of austenite and martensite phase of Fe-25Ni-0.2C alloys, since the austenite specimen consists of martensite phase up to a fraction of 0.25 \pm 0.01 as mentioned in section 4.1.

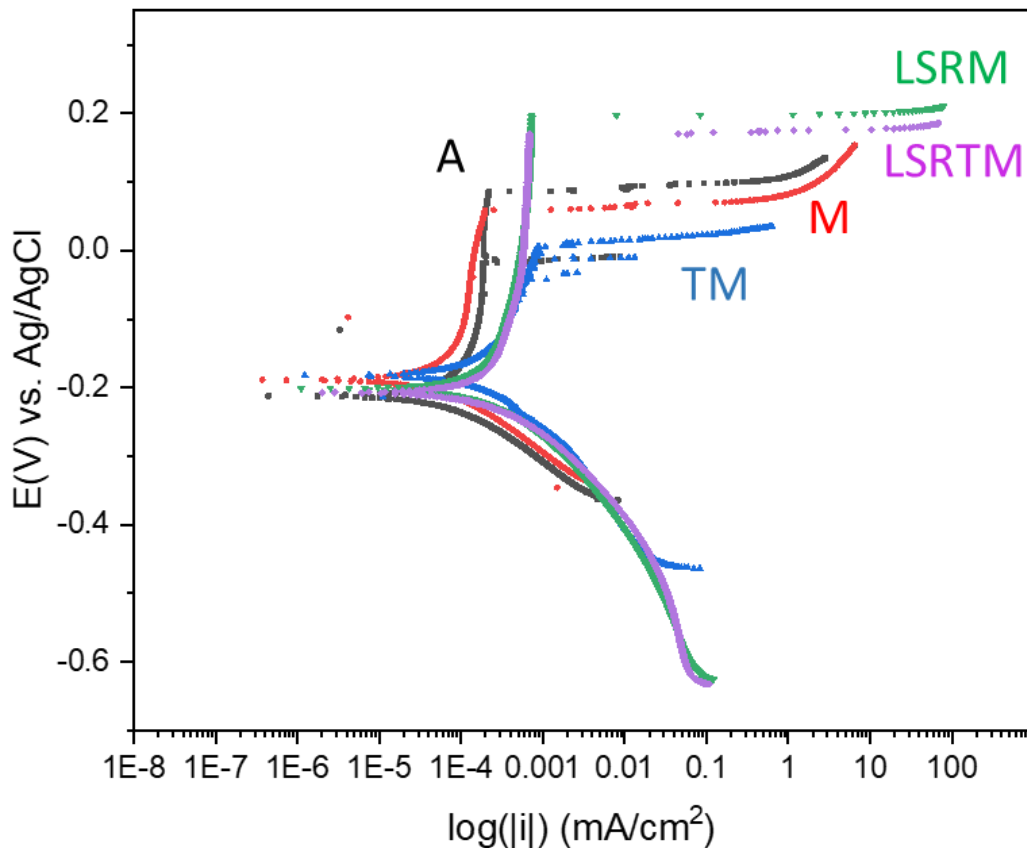


Figure 4.9 Polarization curves of all specimens in 3.5 % NaCl solution (vs. Ag/AgCl)

After laser application (laser line 8: P=160 W, v =200 mms⁻¹), the pitting potential has shifted to a more noble direction, recording 0.153 V_{Ag/AgCl} and 0.162 V_{Ag/AgCl} for lasered martensite and lasered tempered martensite, which is an increase of 0.095 V and 0.140 V, respectively. The passivation interval has also increased from 0.241 to 0.372 V_{Ag/AgCl} for martensite and 0.213 to 0.409 V_{Ag/AgCl} for tempered martensite after the laser treatment, indicating the stability of passivated film has improved. The corrosion data has suggested that the laser treatment has enhanced the pitting corrosion resistance of Fe-25Ni-0.2C.

versus Ag/AgCl	Austenite	Martensite	Tempered Martensite	Lasered Martensite	Lasered Tempered Martensite
E _{corr} (V)	-0.201 ± 0.001	-0.183 ± 0.021	-0.191 ± 0.057	-0.219 ± 0.019	-0.247 ± 0.032
i _{corr} (μA/cm ²)	0.082 ± 0.001	0.073 ± 0.025	0.120 ± 0.054	0.255 ± 0.001	0.509 ± 0.208
E _{pitt} (V)	0.074 ± 0.012	0.058 ± 0.018	0.022 ± 0.016	0.153 ± 0.030	0.162 ± 0.010
E _{pitt} -E _{corr} (V)	0.275 ± 0.021	0.241 ± 0.031	0.213 ± 0.063	0.372 ± 0.011	0.409 ± 0.020
R _{corr} (mmpy)	9.3 × 10 ⁻⁴	8.3 × 10 ⁻⁴	1.4 × 10 ⁻³	2.9 × 10 ⁻³	5.8 × 10 ⁻³

Table 4.2 Mean values of parameters (± standard deviation) from polarization curves in 3.5 % NaCl solution (vs. Ag/AgCl)

From Table 4.2, the i_{corr} has increased significantly, for both martensite and tempered martensite after the laser treatment, which indicates that the general corrosion resistance has reduced for the lasered specimen. The parameter, i_{corr}, can be used to determine the average corrosion rates (R_{corr}) through the following equation [82]:

$$R_{\text{corr}} (\text{mm/year or mmpy}) = 3.27 \times 10^{-3} \times \frac{i_{\text{corr}}}{\rho} \times E_w$$

where i_{corr} is the corrosion current density in the unit of μA/cm², ρ (in g/cm³) is the density of the alloy, and E_w is the equivalent weight of the alloy. For simplicity, the parameters were calculated based on the composition of Fe-25Ni, and the calculated density is 8.13 and the equivalent weight is 28.26 amu.

It is worth mentioning that the area of the lasered specimens is set to be 0.79 mm² (diameter: 1 mm) for the corrosion test, which includes the microstructure of bulk martensite and laser-affected zone and corresponds to around 53% of the overall area percentage of LAZ. The increase in current density can be a result of the galvanic effect which correlates to difference in electrochemical potentials between the surface of reverted austenite and martensite.

The micro-galvanic effect between different phases of the same composition has been reported by Chen et al. [13], who conducted a uniaxial tensile test on austenitic 304 L stainless steel to induce localized plastic deformation, leading to the formation of strain-induced martensite in the parent austenite matrix. The results of scanning Kelvin probe force microscopy (SKPFM) revealed that there was a difference of ~ 60 mV in Volta potential between austenite (higher) and strain-induced martensite (lower), and the Volta potential gradients can lead to microscale galvanic corrosion, which was confirmed by Scanning Electrochemical Microscope (SECM) that strain-induced

martensite has higher surface reactivity than austenite. The finding indicates that diffusion-less microstructural transformations, which result in no compositional change, can lead to changes in localized electrochemical potentials. Similar results of SKPFM have been reported by Korkh et al. [83], which a difference in Volta potentials exists between austenite and strain-induced martensite formed by cold rolling.

The same micro-galvanic effect between austenite and martensite is expected for austenite and martensite specimens. Based on the findings [13, 83], the martensite phase has a lower Volta potential and higher reactivity, which preferentially corrodes as the anode, while the austenite phase acts as the cathode and the oxygen reduction reaction occurs. The cathode/anode area ratio [84] has been reported as an important geometrical factor that determines the galvanic current. An increase in the cathodic area, which is the austenite phase in this situation, leads to more oxygen adsorption on the cathodic surface, and accordingly the oxygen reduction rate increases. Consequently, the dissolution (anodic) reaction is accelerated to provide more electrons for oxygen reduction, resulting in a higher galvanic current. The austenite specimen has a 0.75 ± 0.01 fraction of austenite phase, and its cathode/anode area ratio is higher than the martensite specimen that has a 0.08 ± 0.01 fraction of austenite phase, and this explains the higher current density recorded by the austenite specimen, as shown in Table 4.2.

The effect of tempering treatment on the microstructure of martensite specimen has been characterized in section 4.1, which precipitation of nanoscale carbides is observed in the SEM micrograph in Figure 4.2 (b). Volta potential difference at the carbide/matrix interface has also been reported [85]. Due to the difference in the composition between carbide and matrix material, surface potential gradient emerges as the reactivity is different between phases, and micro-galvanic corrosion that is detrimental to corrosion behavior occurs, leading to an increase in current density and corrosion rate for martensite specimen after tempering treatment, as listed in Table 4.2.

However, the effect of cathode-to-anode ratio on the resulting corrosion rate shows inconsistency when comparing the non-lasered and lasered specimens. The order of cathode-to-anode area ratio from high to low is austenite specimen-lasered martensite specimen-martensite specimen, but the highest corrosion rate is recorded by the lasered martensite specimen. Firstly, near the interface of reverted austenite and martensite, stress is expected to develop during the laser treatment due to volumetric dilatation, which results from the difference in thermal expansion coefficients [31, 33], and it provides an additional driving force for the formation of martensite. Due to structural change, the emergence of corrosion potential gradient between reverted austenite (cathode) and martensite (anode) near the interface is expected, which can lead to micro-galvanic corrosion, as mentioned in the previous paragraph. Secondly, in the base martensite zone that is not affected by laser heat, the phase fraction of the microstructure is the same as the martensite specimen, and hence the same micro-galvanic corrosion between austenite (cathode) and martensite (anode) can take place. Thirdly, at macroscale, the lasered martensite specimen has a phase distribution of bulk martensite (anode)-reverted austenite (cathode) -bulk martensite (anode), and macro-galvanic couples between dissimilar phases also contribute to the increase in corrosion rate. Combined micro and

macro galvanic effect [86] can be the reason for the increase in corrosion rates of martensite after the laser treatment (2.49 times more), and results in the highest corrosion rate despite its intermediate cathode-to-anode area ratio. The schematic of galvanic couplings of lasered martensite is shown in Figure 4.10. The description in black refers to the galvanic corrosion between the bulk martensite (anode) and the laser-reverted austenite (cathode) in the LAZ at macroscale, while the description in red refers to the galvanic corrosion at microscale that can occur at the interface and between butterfly martensite and austenite phases within the bulk martensite, as illustrated in the white scheme at the bottom right corner of Figure 4.10.

The lasered tempered martensite specimen, which has a phase distribution of bulk tempered martensite (anode)-reverted austenite (cathode)-bulk tempered martensite (anode), records a much higher current density than the lasered martensite specimen, as seen in Table 4.2. For microgalvanic effect, tempering treatment intensifies the galvanic corrosion due to carbide precipitation as discussed previously; The galvanic couple between the bulk tempered martensite (anode) and reverted austenite (cathode) is more microstructurally and compositionally inhomogeneous, which leads to a higher electrochemical potential gradient than the couple between bulk martensite and reverted austenite. As a result, the corrosion rate of the tempered martensite specimen is approximately 3 times more after the lasered treatment.

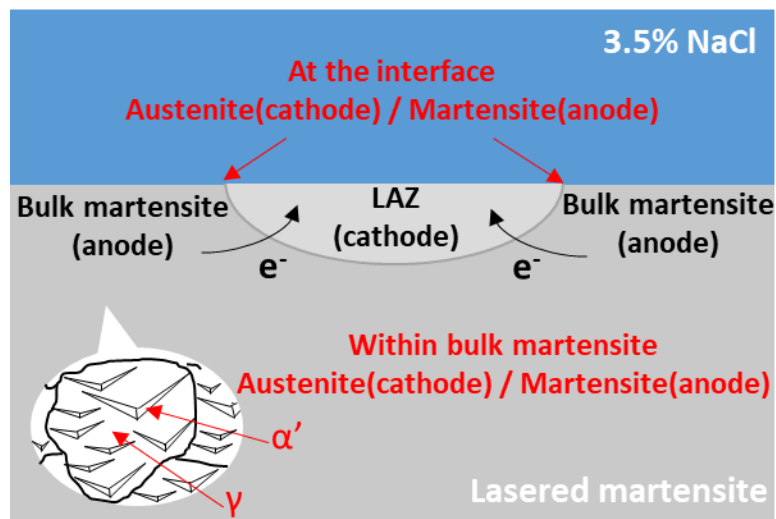


Figure 4.10 Schematic of galvanic couplings of lasered martensite (white scheme at bottom left corner: a simplified representation of bulk microstructure of austenite and butterfly martensite)

4.3.3 Surface Morphological Examination after Corrosion Test

The surface of all specimens has been investigated after the potentiodynamic polarization tests. The optical microscope images of austenite, martensite and tempered martensite (with an exposed area of 6 mm in diameter) are shown in Figure 4.11. 3D profile measurements are utilized for the identification of the propagated pits, which is in the form of a depth color map, and the depth of each pit is measured. The OM images of lasered martensite and lasered tempered martensite (with an exposed area of 1 mm in diameter) are shown in Figure 4.12. In addition to pitting potential, as

discussed in section 4.3.2, other parameters such as density of the pits (number of pits per unit area) and the propagation rate, which determines the depth of pits, are used to assess the resistance to localized pitting. The calculated parameters are listed in Table 4.3.

	Austenite	Martensite	Tempered Martensite	Lasered Martensite	Lasered Tempered Martensite
Exposed area	0.283 cm ² (diameter of 6 mm)			0.0079 cm ² (diameter of 1 mm)	
Pit density (1/cm ²)	7.06	31.8	77.7	253.2	126.6
Pit depth (μm)	53.51 ± 1.39	64.19 ± 9.20	89.72 ± 15.27	18.5 ± 9.19	36

Table 4.3 Pitting corrosion parameters for all specimens

From Figure 4.11 (a) and (c), the phenomenon of metastable pits can be observed for austenite and tempered martensite, which results in the appearance of dark and brownish micron-sized dots on the surface. This morphological result corresponds to the fluctuation of current density below the critical pitting potential in Figure 4.9 in section 4.3.2. These metastable pits have a limited lifetime of seconds because within the pits, the condition of concentrated acidic chloride solution (anolyte) that propagates the pits is not maintained, and the metastable pits repassivate [48]. The aggressive anolyte inside the pit is acidic due to the hydrolysis reaction of the dissolving iron cations and is high in the concentration of chloride anions resulting from charge neutrality. Based on the finding of Pistorius and Burstein [87], for the metastable pits to further grow stably, the pits require a perforated cover [87] as barrier to ion diffusion to maintain the aggressive anolyte, and then grow to a certain depth that the pit depth itself could serve as diffusion barrier. If the cover ruptures prematurely, the anolyte is diluted and the repassivation occurs. In this work, the repassivation of metastable pits are further characterized by SEM and EDS, which will be discussed in the following section.

From Table 4.3, both the rankings of pit density and pit depth (in descending order) are tempered martensite > martensite > austenite, which indicates that the austenite specimen is the most pitting corrosion resistant, and the tempered martensite specimen is the most susceptible to pitting. This morphological result is consistent with the results obtained from polarization curves in Table 4.2. The onset of pit initiation and growth is least favorable for the austenite specimen as its pitting potential (E_{pit}) is the highest. This can be attributed to its higher fraction of the austenite phase, and results in a formation of more stable passive film on the surface of austenite specimen as its passivation interval ($E_{pit} - E_{corr}$) is the highest. The finding of Bösing et al. [88], who investigated the effect of strain-induced martensite content on AISI 304 austenitic stainless steel's passivation behavior, also suggested that the stability of the passive layer increases with increasing austenite content. Higher martensite content decreases the polarization resistance and increases the concentration of point defects, which indicates its passive film is thinner and less homogeneous, and hence less stable. The increased susceptibility of the tempered martensite specimen to pitting corrosion is due to the precipitation of carbides, as mentioned before.

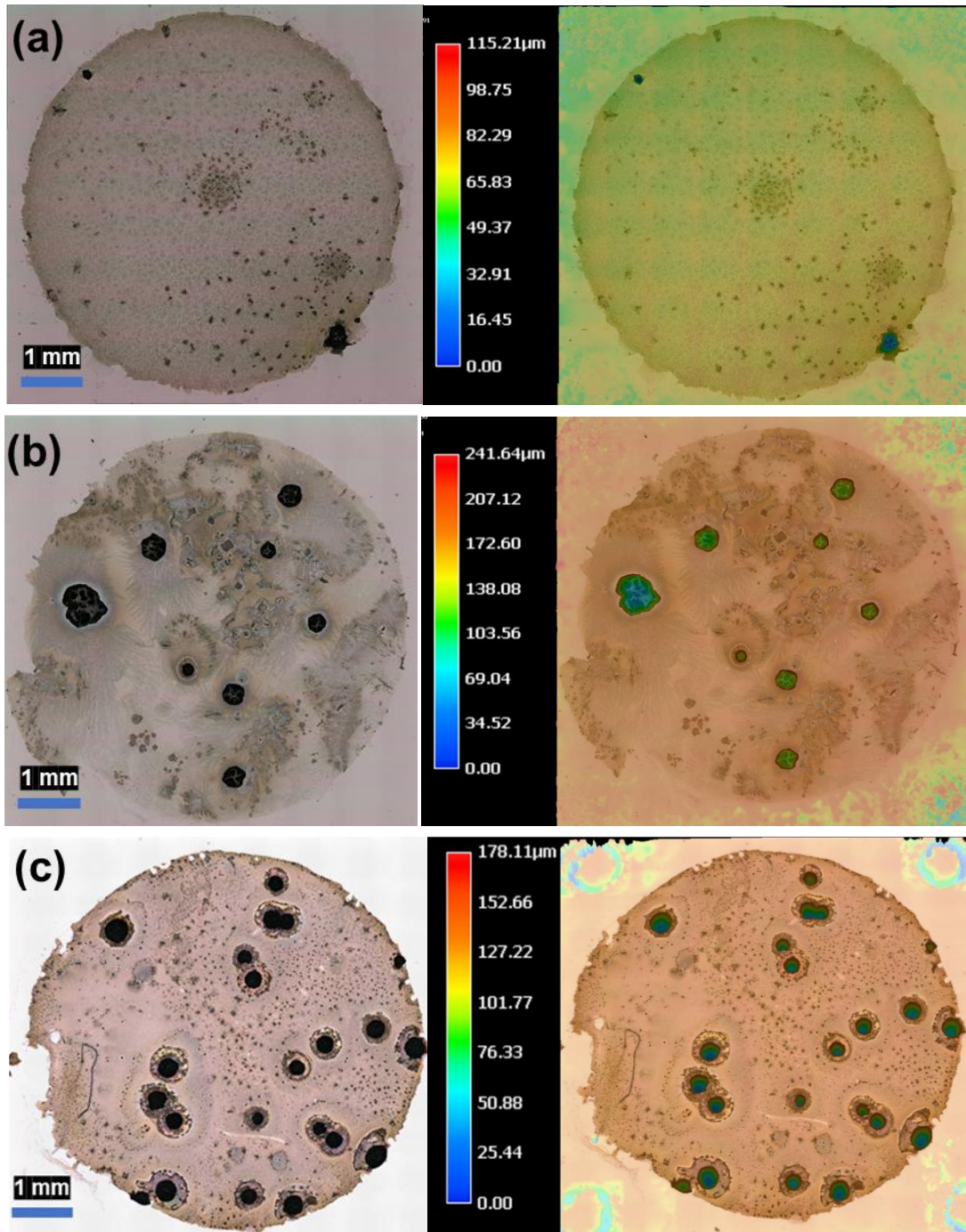


Figure 4.11 Optical microscope images and their corresponding depth color maps of surface of (a) austenite, (b) martensite and (c) tempered martensite specimens after potentiodynamic polarization test in 3.5% NaCl

After the laser treatment, the martensite and the tempered martensite specimen record potential shifts of 0.095 V and 0.14 V, respectively, in a more noble direction. The improvement in pitting corrosion resistance for both specimens can also be observed from the surface morphological results as the pit depth decreases. However, the pit density has significantly increased, indicating more but shallow pits are formed and distributed on the surface of lasered specimens, unlike the surface of non-lasered specimens that forms deeper but less pits per unit surface area. The pit depth [89] is more susceptible and correlates strongly to the failure of materials, i.e., a material with a surface of fewer but much deeper pits is more likely to fail than that with many but shallow pits. “Local” pitting density, or clustering of pits, is a more important parameter than the “general” pitting density to assess the pitting corrosion behavior, and it shows a strong correlation to the failure of materials [89]. In Figure 4.11 (b) and (c), clustering of pits can be observed on the surface of martensite and tempered martensite that some pits initiate and propagate close to each other, and eventually merge.

The improvement in pitting corrosion resistance is due to the martensite-to-austenite reversion caused by laser treatment, which increases the austenite phase content, and leads to higher passivation intervals. However, the fraction of the austenite phase of the laser-treated specimen is lower than that of the austenite specimen but shows better pitting corrosion resistance. As mentioned in section 4.3, the reverted austenite is formed through the austenite memory effect, which has the same grain shape and orientation as prior austenite but much higher dislocation density, and in this work, the grain size of laser-reverted austenite is measured to be larger, indicating the difference in microstructural properties, which might contribute to the enhancement of corrosion behavior.

According to Gaberšček and Pejovnik [90], the metal surface is non-passivated at the moment of the immersion in the electrolyte, and the passive film would preferentially grow at the most favorable (active) sites after an induction time, when the energy of the active sites exceeds a critical value, and then gradually spread over the metal surface. The active sites include the surface defects, such as dislocations, grain boundaries, inclusions [91, 92], etc. The preferential dissolution at the dislocation is further confirmed by Zhang and Ma through TEM analysis [93]. The standard electrode potential (SEP) was found to drop drastically in the region around the dislocation core. The structural defects induced heterogeneity in electrode potentials, which is the driving force to initiate the dissolution.

Li et al. [92] investigated the passive film formed on nanocrystalline and coarse-grained stainless steel. The finding shows that the large fraction of closely spaced surface defects, which are grain boundaries and grain boundary triple junction, of nanocrystalline stainless steel leads to instantaneous nucleation of passive film at these active sites, and then spreads over the surface to connect each to form a uniform passive layer that significantly improves the pitting behavior. The closely spaced surface defects shorten the lateral distance required for lateral growth of a uniform passive layer. The absence of inclusions in nanocrystalline stainless steel is also reported to contribute to the better corrosion performance.

Man et al. [91] investigated the effect of selective laser melting (SLM) on the passive and pitting behavior of 316L stainless steel (316L SS). Both SLM and wrought 316L are pure austenite with similar averaged grain size, but the SLM specimen has a much higher grain boundary length, which is related to its curvier grain boundary shape, and much higher dislocation density due to high residual stress introduced by the rapid solidification rate during laser. The passive film formed on SLM 316L is thicker and hence more protective. In addition to the effect of higher surface defects, the reduction in inclusion size due to refinement induced by laser treatment also plays a role in improving the pitting corrosion resistance.

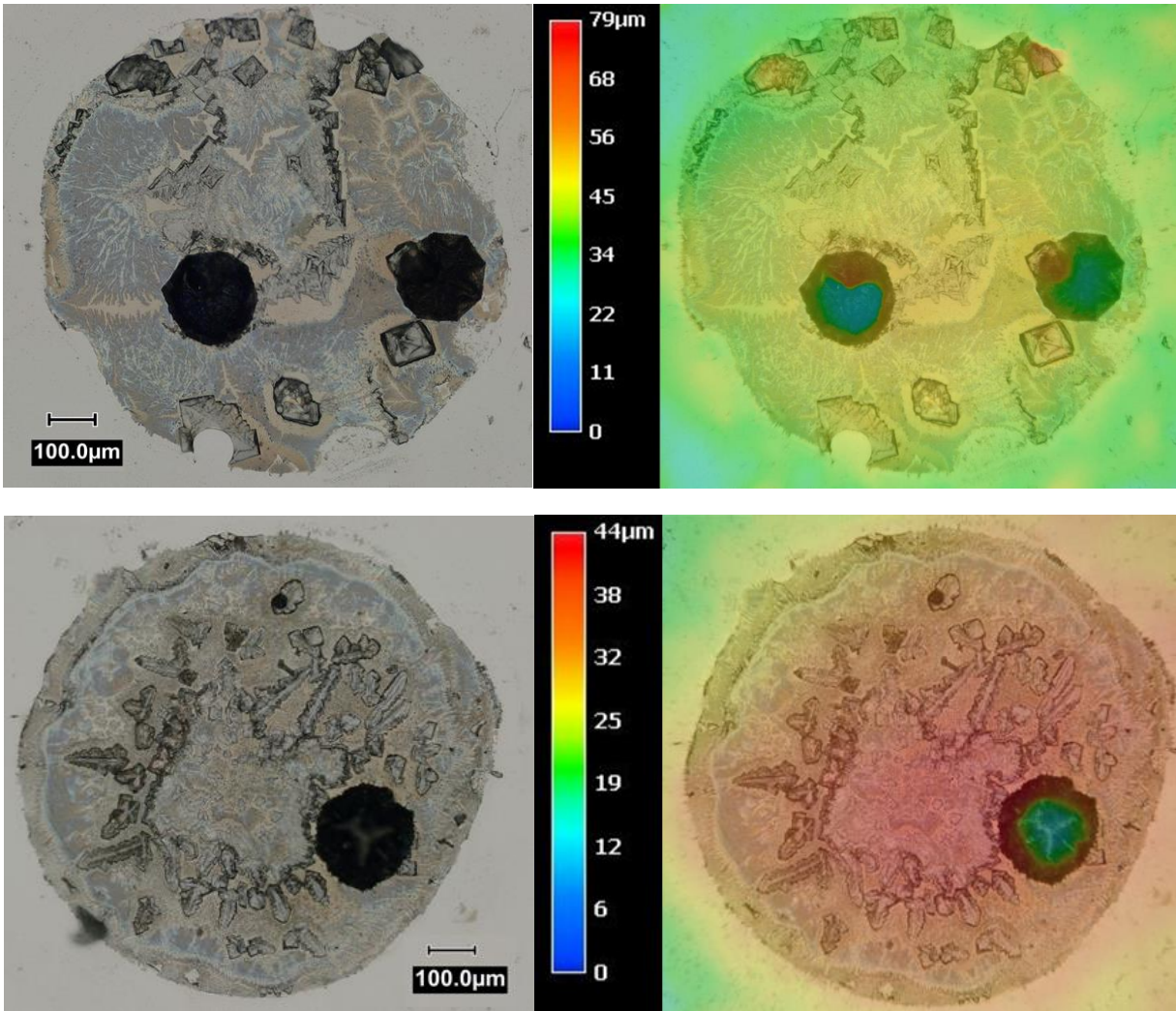


Figure 4.12 Optical microscope images and their corresponding depth color maps of surface of (a) lasered martensite and (b) lasered tempered martensite after potentiodynamic polarization test in 3.5% NaCl

In conclusion, besides the microstructural transformation caused by laser treatment that increases the austenite phase fraction, the higher dislocation density of the lasered-reverted austenite than prior austenite might further improve the stability of passive film through the mechanism

mentioned previously. The possible refinement or elimination of inclusions and precipitates in the matrix during laser treatment, which is not characterized in this work, can enhance the chemical homogeneity that also leads to better pitting corrosion resistance. As stated, those surface defects serve as preferable initiation sites for passive film, however, during the further coverage process of the surface the film already formed may undergo significant changes in its microstructural and electrical properties [90]. This indicates the complexity of the entire passivation and pitting process. The enhanced stability of the passive film after laser treatment can be a result of higher thickness or better homogeneity of passive films. Further test and characterization, such as electrochemical impedance spectroscopy (EIS) and Mott-Schottky Analysis [88], is required to fully understand the formation mechanism and properties of the passive films.

4.3.4 Scanning Electron Microscope (SEM)-Energy Dispersive X-ray Spectroscopy (EDS)

Following the potentiodynamic polarization test, SEM analysis were carried out for more detailed morphology of the pits as well as the specimen surface. EDS measurement was used to obtain corresponding qualitative data for detection or identification of the elements and semi-quantitative data for approximation of the concentration of elements in the material. EDS can detect major elements with concentrations higher than 10 wt.% and minor elements with concentrations between 1 and 10 wt.% [94]. The detection limit of EDS for bulk materials is 0.1 wt.%. Therefore, for the material of this research, Fe-25Ni-0.2C, composition of which is shown in Table 3.1, the detection of element Fe and Ni is expected, while the peak of carbon (0.2 wt.%) that is corresponding to K_{α} value of 0.277 keV and other elements in the material, might not be detectable.

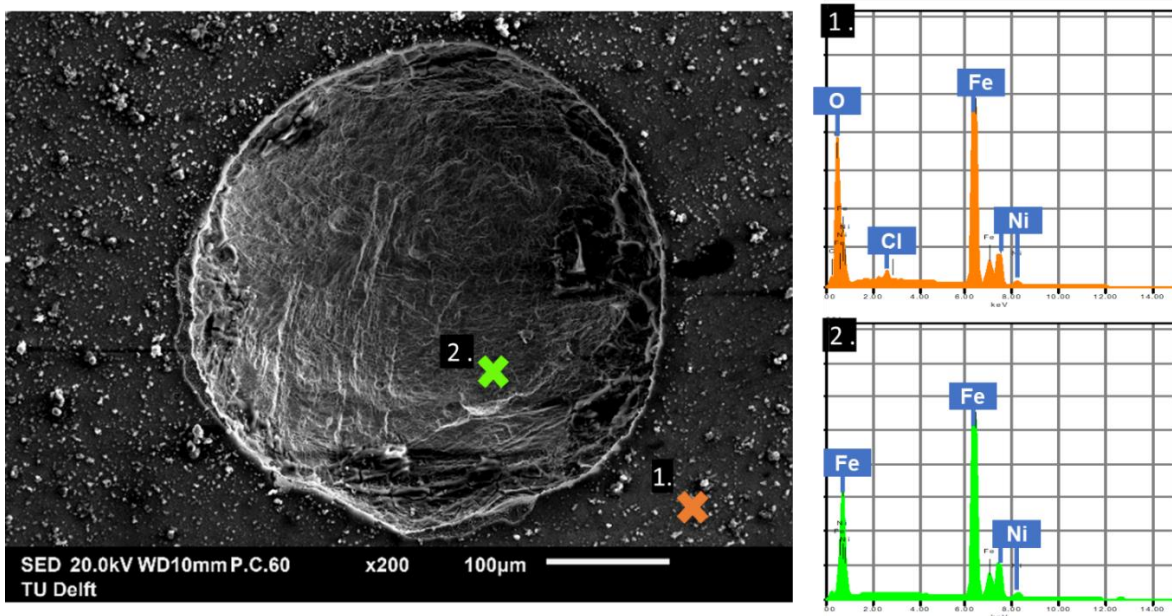


Figure 4.13 SEM micrograph of the pit on the martensite surface after potentiodynamic polarization test in 3.5% NaCl, and its corresponding EDS profile of inside-the-pit (marked as green cross) and the surface position (marked as orange cross)

Unit: wt.%	Fe	Ni	O	Cl
Point 1	68.13	17.49	13.21	1.16
Point 2	78.57	21.43	-	-

Table 4.4 Corresponding weight percentages of elements detected in Figure 4.13

Figure 4.13 displays the SEM micrograph of the pit on the surface of martensite after the corrosion test and its corresponding EDS analysis. The EDS analysis was conducted at both spots of inside-the-pit (marked as a green cross, point 2) and the surface near the pit (marked as an orange cross, point 1). The shape of the pit appears to be wide and shallow with a width of nearly 390 μm and a depth of nearly 65 μm . The characteristic peaks of iron (K_{α} : 0.277 keV), nickel (K_{α} : 7.417 keV), oxygen (K_{α} : 0.525 keV) and chloride (K_{α} : 2.621 keV) can be detected for the spot at the surface, and the corresponding weight percentages of the elements detected were as follows: 68.13 wt.% Fe, 17.49 wt.% Ni, 13.21 wt.% O and 1.16 wt.% Cl. The presence of oxygen indicates the existence of oxides as a corrosion product on the surface, which can provide protection to the alloy surface against further corrosion attack. The relatively low weight percentages of iron (68.13 wt.%) and nickel (17.49 wt.%) compared to the original composition of the alloy can be attributed to the formation of a thick layer of corrosion products, which covers and protects the original surface of the alloy underneath [55]. According to the Fe–Ni composite Pourbaix diagram shown in Figure 2.11, as the pH value remains around neutral for positions outside the pits, this thick layer most likely contains $\text{Fe}_2\text{O}_{3(s)}$. In addition, the presence of Cl (1.16 wt.%) suggests that the corrosion products might not only form as oxides but also possible chloride compounds [81]. The possibility of the contribution of residual NaCl salts from the electrolyte to the Cl signal can be ruled out because no Na peak (K_{α} : 1.041 keV) is detected. Instead, the NaCl salts deposited on the surface would appear in the morphology of cubic particles, as shown in Figure 4.14, and the peak of Na is distinct. The weight percentages are 37.86 wt.% Na and 62.14 wt.% Cl, and the corresponding atomic percentages are 48.5 at.% Na and 51.5 at.% Cl, which is close to atomic ratio of 1:1.

The elements detected within the pit (marked as green cross, point 2) are Fe and Ni only, and no signal of O or Cl is present. The weight percentage is 78.57 wt.% Fe and 21.43 wt.% Ni, which is comparable to the original composition of Fe-25Ni-0.2C. Similar to the result of NaCl, the EDS semi-quantitative analysis provides an approximate concentration of detected elements. Comparing the qualitative result of the elements within and near the pit, it suggests that the surface near the pit is covered by a protective layer of oxide and possible chloride compounds, which is a result of the cathodic reaction, and within the pit, the anodic dissolution takes place, leading to exposure of the bulk material underneath the protective layer, and hence EDS result is close to the original composition of the alloy.

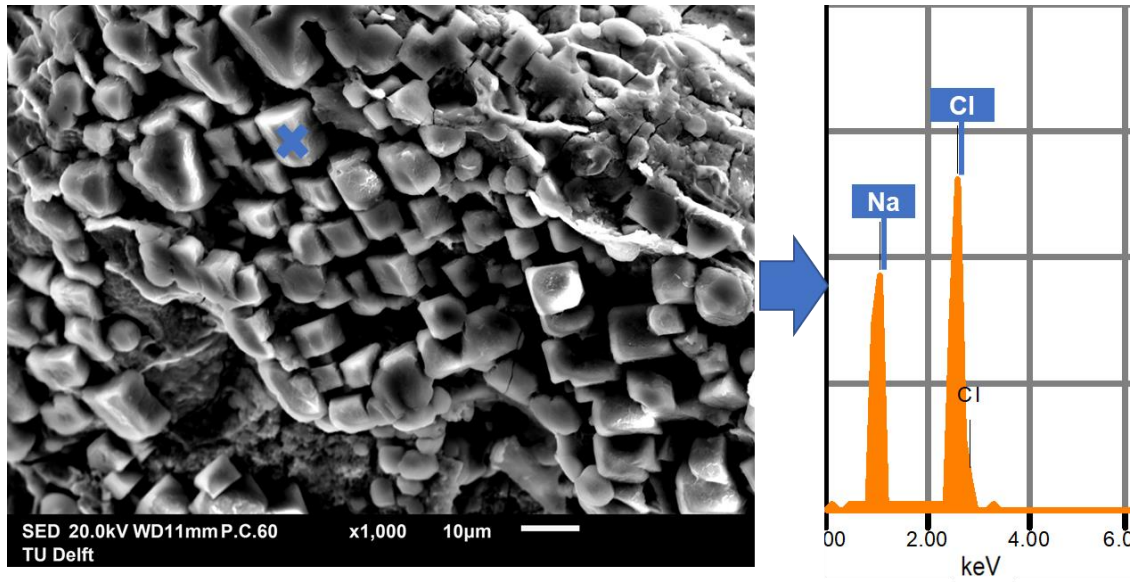


Figure 4.14 SEM micrograph of residual NaCl salts deposited on the surface after potentiodynamic polarization test in 3.5% NaCl, and its corresponding EDS profile

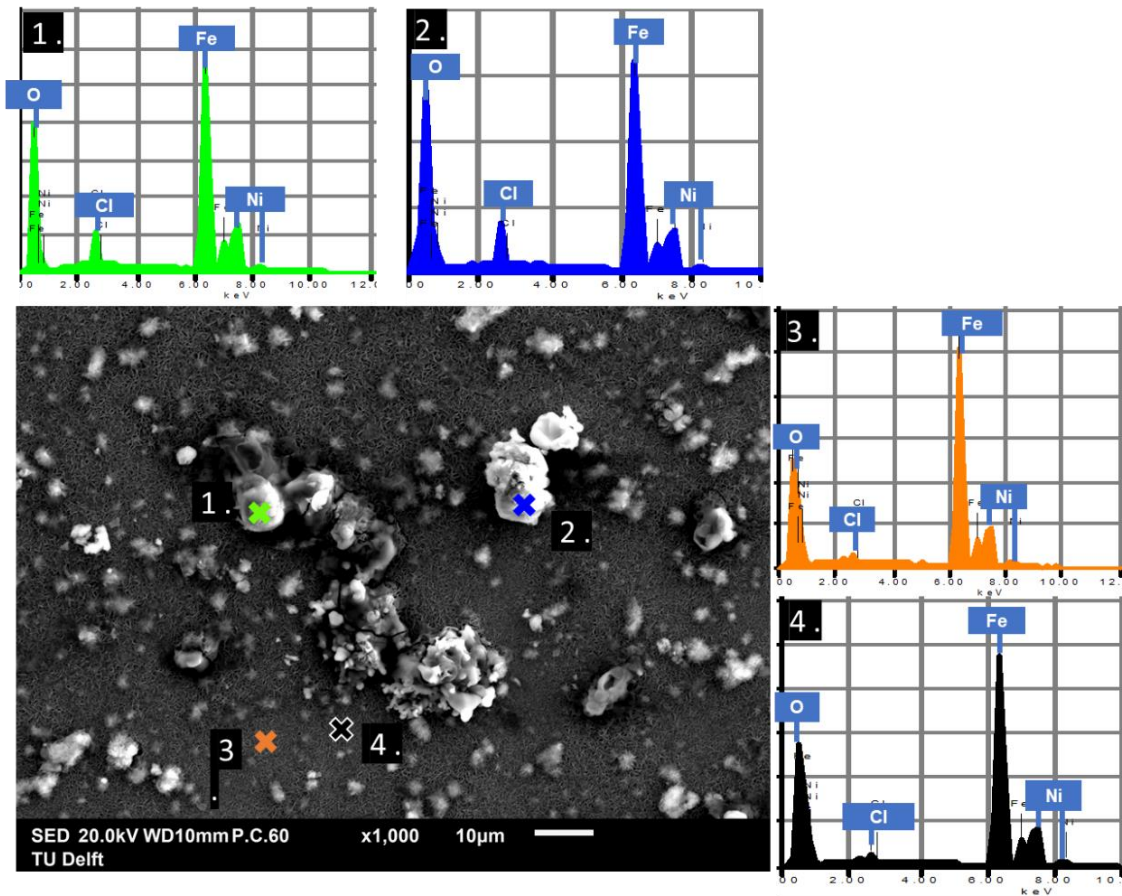


Figure 4.15 SEM micrograph of the surface of martensite after potentiodynamic polarization test in 3.5% NaCl, and its corresponding EDS profile

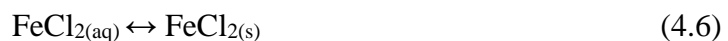
Unit: wt. %	Fe	Ni	O	Cl
Point 1	61.06	18.54	17.61	2.79
Point 2	58.51	17.38	20.79	3.32
Point 3	67.35	17.17	14.71	0.76
Point 4	68.10	18.46	12.84	0.59

Table 4.5 Corresponding weight percentages of elements detected in Figure 4.15

More detailed SEM images of the martensite surface after corrosion is presented in Figure 4.15. Part of the surface is covered with corrosion product that appears as lighter grey compounds in the image. For EDS analysis, four points are selected, which are two points on the corrosion product and two on the surface without deposited compounds. From the qualitative results, signals of Fe, Ni, O and Cl are detected for all four points, and the corresponding weight percentages of the elements are presented in Table 4.5. The presence of oxygen (with more than 10 wt.%) suggests that the layer of oxides is formed as a corrosion product and covers the original surface of the alloy, resulting in the relatively low percentages of Fe and Ni detected compared to its original composition. Comparing the results, it can be observed that the weight percentages of Fe are lower, and O and Cl are higher at points 1 and 2, while Ni is relatively constant (17-18 wt.%) throughout the four measured points. The result of higher oxygen content suggests that the corrosion product is thicker at points 1 and 2, which is consistent with the observation of microstructure from the SEM image. In addition, the lower percentage of iron and the relatively fixed concentration of nickel at points 1 and 2 suggests that the dissolution (anodic) reaction of the alloy most likely occurs through the dissolution of Fe, as mentioned in section 4.3.2, and forms a protective layer of iron oxides and possible iron chloride.

The morphological analysis of the surface of austenite after the corrosion test in 3.5% NaCl is also conducted. The SEM image and its corresponding EDS results are present in Figure 4.16 and Table 4.6. The surface selected corresponds to the area with metastable pits that appear as dark brown micron-size spots in Figure 4.16 (a). The presence of oxygen and low percentages of Fe and Ni indicates the original surface is covered with oxides. The lower percentages of Fe and Ni at point 1 and 2 is due to thicker corrosion product formed on the surface than at point 3 and 4, and high percentages of Cl detected for point 1 (20.37 wt.%) and 2 (15.3 wt.%) suggest that the corrosion product might contain chloride, while the Cl as well as Na detected at point 3 and 4 is mostly contributed by residual NaCl from the electrolyte.

The high concentration of chloride might be contributed by iron chloride (FeCl_2). The iron chloride can be formed as follows [53]:



The Fe^{2+} ion is generated by the anodic dissolution of iron inside the pit, and it reacts with Cl^- that migrate to the anodic site due to charge neutrality to form $\text{FeCl}_{2(\text{aq})}$. When the concentration of highly soluble iron chloride reaches saturation, $\text{FeCl}_{2(\text{s})}$ will precipitate. The mechanism of

repassivation of metastable pits is not certain, but it is suggested that salt films are formed at the base of the metastable pits and protect the metal from further pit growth [48]. Rayment et al. [95]. utilized X-ray diffraction to characterize the salt film formed on dissolving iron surface in artificial corrosion pits in 1 M HCl, which is a highly concentrated acidic chloride solution as in real pits, and the result showed that the salt film is predominantly $\text{FeCl}_2 \cdot 4\text{H}_2\text{O}$.

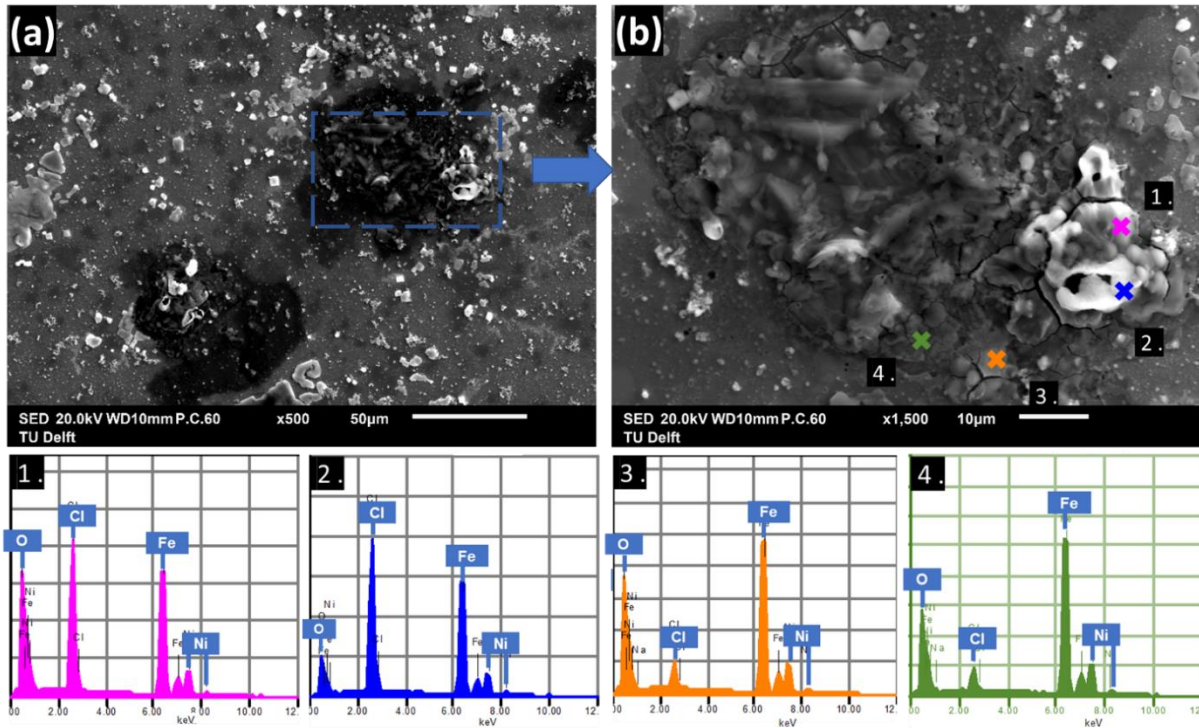


Figure 4.16 (a) SEM micrograph of the surface of austenite after potentiodynamic polarization test in 3.5% NaCl (b) Higher-magnification SEM micrograph of the area (marked with blue dashed line) and its corresponding EDS profile

Unit: wt.%	Fe	Ni	O	Na	Cl
Point 1	54.99	13.02	11.62	-	20.37
Point 2	48.34	12.44	23.92	-	15.30
Point 3	61.23	16.20	18.75	1.04	2.77
Point 4	64.21	17.62	13.72	1.74	2.72

Table 4.6 Corresponding weight percentages of elements detected in Figure 4.16 (b)

The SEM micrographs of the two pits of lasered martensite (LSRM) are shown in Figure 4.17, where the depth of pit in (a) is 25 μm and in (b) is 12 μm . Oxygen is detected for all four points detected as shown in Table 4.7, which results from the formation of oxide on the surface. A high weight percentage of Cl (17.15 wt.%) is detected within the pit site (point 1) with the relatively low percentage of Na (3.04 wt.%), where theoretically for NaCl the mass ratio of Na to Cl is 39.33% to 60.67%, which indicates that the signal of Cl is contributed by both NaCl and possible iron chloride. The EDS results at point 2 show that residual NaCl from the electrolyte is deposited and

covering the surface, leading to low weight percentages of iron (2.48 wt.%) and nickel (0.79 wt.%), which is similar to the finding of point 4 in Figure 4.17 (b).

The edge and vicinity of the 36- μm -deep pit of lasered tempered martensite (LSRTM) are covered with many residual sodium chloride particles, as shown in Figure 4.18. Both spots analyzed by EDS show a peak of iron, nickel and oxygen, while only spot 2 (position within the pit) show the signal of chloride.

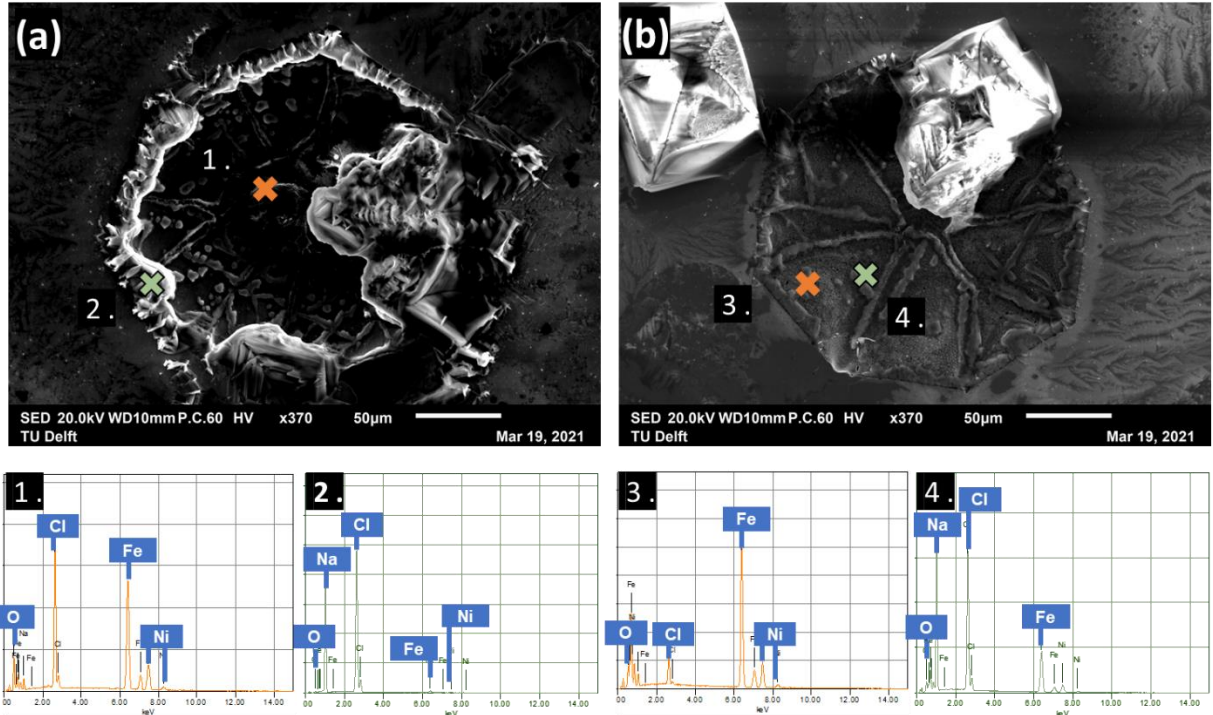


Figure 4.17 (a) and (b) SEM micrographs of the two pits of lasered martensite after potentiodynamic polarization test in 3.5% NaCl, and its corresponding EDS profile

Unit: wt.%	Fe	Ni	O	Na	Cl
Point 1	52.85	18.15	8.80	3.04	17.15
Point 2	2.48	0.79	2.09	37.65	56.99
Point 3	69.13	19.48	3.76	4.07	3.56
Point 4	28.49	7.10	4.69	34.39	25.33

Table 4.7 Corresponding weight percentages of elements detected in Figure 4.17

Comparing the EDS data prior to and after the laser treatment, the quantitative result within the pit of martensite shows composition close to the original composition of the material with no signals of oxygen and chloride, as shown for point 2 in Table 4.4. For lasered martensite specimens, oxygen, as well as chloride, are present within the pits, as shown for points 1, 3 and 4 in Table 4.7, indicating oxide formation or salt film precipitation on the pit walls. However, not much information can be extracted since the structure of the precipitated salt film is uncertain. The porosity and thickness are reported to be the governing factors for the mechanism of ionic transport through it [81]. The

porous film indicates a low field-transport process, which has been reported for both nickel and stainless steel by Hunkeler et al. [60]. Whatever the structure of the precipitation film is formed on the pit wall, the pit propagation of lasered martensite specimen is harder than the martensite specimen since the diffusion of ions is hindered by the film. The schematics of pitting corrosion of the martensite and the lasered martensite specimens are shown in Figure 4.19 and Figure 4.20, respectively.

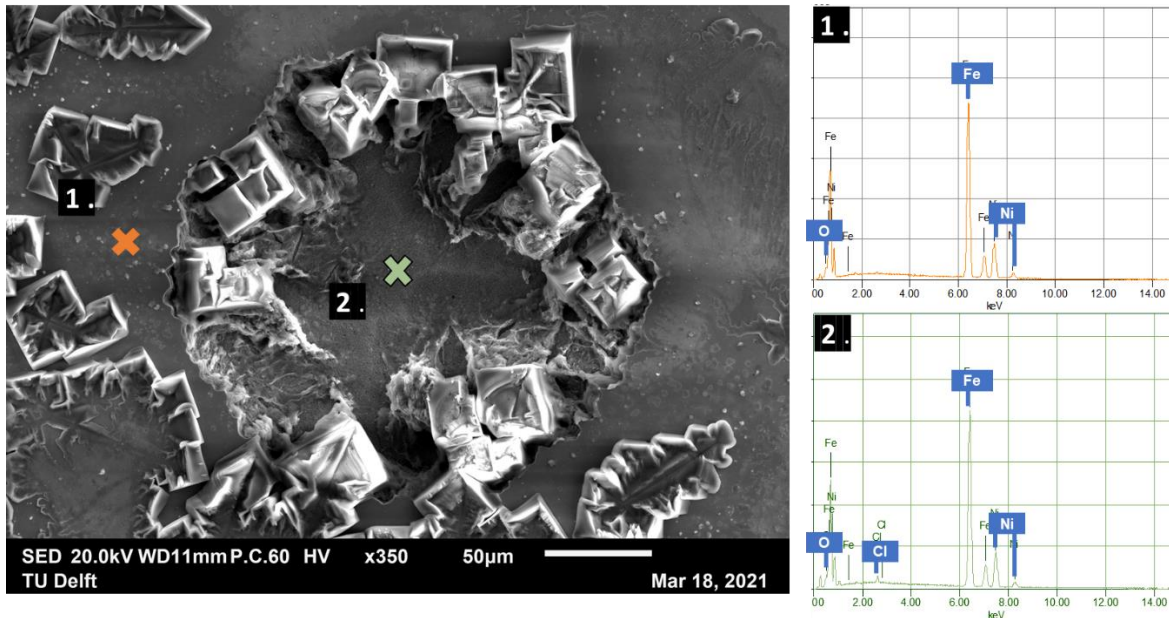


Figure 4.18 SEM micrograph of the pit of lasered tempered martensite after potentiodynamic polarization test in 3.5% NaCl, and its corresponding EDS profile

Unit: wt.%	Fe	Ni	O	Cl
Point 1	75.96	23.19	0.85	-
Point 2	75.40	22.59	1.21	0.80

Table 4.8 Corresponding weight percentages of elements detected in Figure 4.18

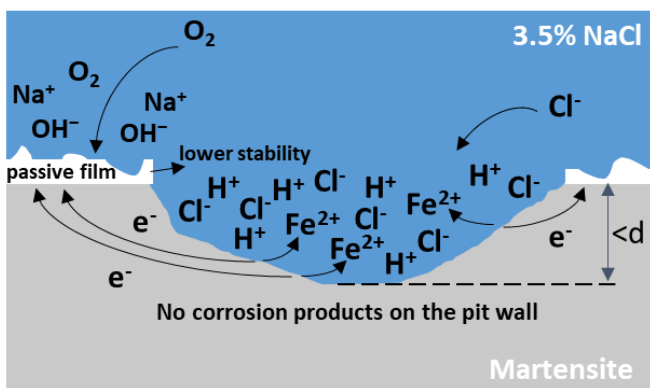


Figure 4.19 Schematic of pitting corrosion of martensite specimen (no corrosion products on the pit all)

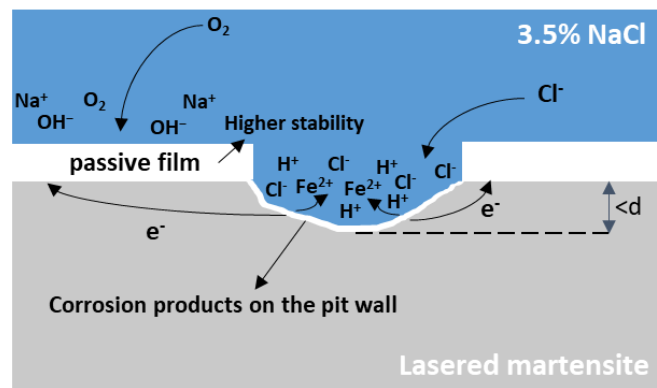


Figure 4.20 Schematic of pitting corrosion of lasered martensite specimen (corrosion products on the pit all)

5. Conclusion

In conclusion, the main findings can be extracted from the results and discussion of this work. The microstructure of lasered affected zone (LAZ) was formed on cryogenically formed martensitic Fe-25Ni-0.2C alloys by continuous-wave Nd:YAG laser system. The microstructural changes and the corrosion behavior of the treated zones were studied. The research approach was as follows:

1. Microstructure
 - a. Microscopy: to analyze the effect of localized laser treatment and localized corrosion on microstructure of Fe-25Ni-0.2C as-quenched austenite, martensite and tempered martensite.
2. Corrosion behavior
 - a. Electrochemical analysis: to assess the corrosion behavior of Fe-25Ni-0.2C alloys prior to and after localized laser treatment.
 - b. Qualitative and semi-quantitative analysis: to characterize the corrosion product and possible corrosion mechanism.

Following the main conclusions obtained from the microstructure and corrosion studies.

Microstructure

1. Initial heat treatment:
 - a. Austenite specimen: an average grain size of $67 \pm 5 \mu\text{m}$ with a weight fraction of the martensite up to $25 \pm 1\%$.
 - b. Martensite specimen: the morphology of butterfly wing and weight fraction of $8 \pm 1\%$ of retained austenite.
 - c. Tempered martensite: carbide precipitation is observed within the butterfly wings.
2. After the localized laser treatment on the bulk martensite, three main distinct microstructural zones can be distinguished:
 - a. Melt zone: micron-scale fine grains with dendritic structure are observed, which is a result of supercooling (undercooling) of the molten alloys prior to solidification.
 - b. Lasered affected zone (LAZ): solid-state martensite-to-austenite reversion occurs, and two distinct regions can be observed within this zone:
 - (i) Fine-grained austenite: in the region near the melting zone. The formation mechanism is through recrystallization due to the high dislocation density, and the newly formed grains show straight grain boundaries.
 - (ii) Coarse-grained austenite: in the region near bulk martensite. The grains with similar size and shape as prior austenite are formed through austenite memory mechanism, and hence shows curvy grain boundaries.

- c. Parent martensite: martensitic microstructure in the bulk that is unaffected by localized laser treatment.
3. The effect of laser parameters of laser power (P) and scanning velocity (v) on the microstructure has been investigated. Both higher laser power, i.e., higher energy input to the materials, and lower scanning velocity, i.e., longer laser-material interaction, lead to a larger dimension of the melting zone, as well as a wider and deeper formation of the LAZ.

Corrosion

1. General corrosion:

Before the localized laser treatment, the corrosion rate of the austenite specimen was higher than the martensite specimen due to its higher cathode-to-anode ratio, which intensifies the galvanic corrosion. The carbide precipitation of the tempered martensite also deteriorates the corrosion resistance. After the laser treatment, the recorded corrosion rate is 2.49 and 3.14 higher for martensite and tempered martensite, respectively. This result can be contributed by both the microscale galvanic couplings at the reverted austenite/ martensite interface and the macroscale galvanic corrosion between the phases.

2. Pitting corrosion:

After the laser treatment, the pitting potential has shifted to a more noble direction by 0.095 and 0.140 $V_{\text{Ag}/\text{AgCl}}$ for martensite and tempered martensite, respectively. The passivation interval ($E_{\text{pit}} - E_{\text{corr}}$) has also increased by 0.131 and 0.196 $V_{\text{Ag}/\text{AgCl}}$, respectively. The enhancement can be attributed to the presence of reverted austenite that has a better pitting resistance, and results in the formation of a more stable passive film.

3. Corrosion products formed on the surface are mainly oxides as high weight percentage of oxygen is detected. At the metastable pits, high chloride content is present, which indicates the mechanism of repassivation might occur through the formation of iron chloride (FeCl_2). After the laser treatment, the results show signals of oxygen and chloride in the pit, indicating the oxide and salt film that hinder ions diffusion are formed on the pit wall. This could be the reason for the formation of shallower pits on the surface of lasered specimens.

In this work, the architected microstructure of reverted austenite/martensite phases was created on cryogenically treated Fe-25Ni-0.2C alloys by laser surface treatment. The microstructure consists of the melt, the lasered affected zone (LAZ), and the base martensite. Laser processing parameters were found to affect the dimension of the LAZ, which increased with increasing laser power (P) and decreasing scanning speed (v). The LAZ can further be distinguished as fine-grained and coarse-grained austenite regions, and the transformation mechanisms are recrystallization and austenite memory, respectively. For corrosion analysis, the current density has increased by nearly 2.5 times for the martensite specimen after the laser treatment. The deteriorated general corrosion resistance can be attributed to the galvanic corrosion between austenite and martensite that occurred at both micro and macro scale. The pitting corrosion resistance has improved as the pitting potentials shifted to more noble direction, which results from better stability of the passive films due to the presence of the austenite phase that has better corrosion resistance over the martensite phase.

6. Recommendation

Some recommendations can be made for future work based on the findings in this work.

1. The laser parameters investigated in this work are laser power (P) and scanning speed (v), and melting is not avoidable even with the lowest laser power density. The focal position, which refers to the distance between the focal plane and the surface of the workpiece, is another parameter that directly influences the laser power density. By increasing the distance, laser spot size increases, and laser power density decreases, indicating a possibility to create a more homogeneous microstructure with only solid-state transformation.
2. The effect of single-pass laser treatment on the formation mechanisms is understood in this work. For further investigation, microstructures formed by multi-pass laser can be an interesting topic.
3. Due to the sample preparation, the surface is removed, and the corrosion test is conducted on the surface with the combination of coarse-grained austenite and bulk martensite. It would be interesting to investigate the effect of recrystallized austenite (fine-grained austenite) on the corrosion behavior as well. Moreover, the area fraction of coarse-grained austenite is fixed at around 50% in this work. Corrosion tests on specimens with different area fractions should be conducted.
4. Obtaining the Volta potentials of different phases with Scanning Kelvin Probe Microscopy (SKPM) is required to confirm the mechanism of galvanic corrosion.
5. The EDS analysis is insufficient to identify the corrosion products. More detailed chemical analysis, such as X-ray photoelectron spectroscopy (XPS) or Auger electron spectroscopy (AES), is advised for identification of the compounds formed during the corrosion process.
6. The improvement in pitting corrosion after the laser treatment is due to the formation of a more stable passive film. More detailed characterization should be carried out, such as electrochemical impedance spectroscopy (EIS) and Mott-Schottky analysis, to reveal the properties and defect density of the passive film.

7. Bibliography

1. Valdevit, L., Bertoldi, K., Guest, J., & Spadaccini, C. (2018). Introduction. *Journal of Materials Research*, 33(3), 241-246. doi:10.1557/jmr.2018.18
2. Thori, P., Sharma, P., & Bhargava, M. (2013). An approach of composite materials in industrial machinery: advantages, disadvantages and applications. *International Journal of Research in Engineering and Technology*, 2(12), 350-355.
3. Sugimoto, K. I., Kobayashi, M., & Hashimoto, S. I. (1992). Ductility and strain-induced transformation in a high-strength transformation-induced plasticity-aided dual-phase steel. *Metallurgical Transactions A*, 23(11), 3085-3091..
4. Maxwell, P. C., Goldberg, A., & Shyne, J. C. (1974). Stress-assisted and strain-induced martensites in Fe-Ni-C alloys. *Metallurgical Transactions*, 5(6), 1305-1318..
5. Xu, S. S., Li, J. P., Cui, Y., Zhang, Y., Sun, L. X., Li, J., ... & Zhang, Z. W. (2020). Mechanical properties and deformation mechanisms of a novel austenite-martensite dual phase steel. *International Journal of Plasticity*, 128, 102677.
6. Koyama, M., Tasan, C. C., Nagashima, T., Akiyama, E., Raabe, D., & Tsuzaki, K. (2016). Hydrogen-assisted damage in austenite/martensite dual-phase steel. *Philosophical Magazine Letters*, 96(1), 9-18.
7. Mazumder, J. "Laser heat treatment: the state of the art." *JOM* 35.5 (1983): 18-26.
8. Dinesh Babu, P., Balasubramanian, K. R., & Buvanashakaran, G. (2011). Laser surface hardening: a review. *International Journal of Surface Science and Engineering*, 5(2-3), 131-151.
9. Kwok, C. T., Man, H. C., & Cheng, F. T. (2000). Cavitation erosion and pitting corrosion behaviour of laser surface-melted martensitic stainless steel UNS S42000. *Surface and Coatings Technology*, 126(2-3), 238-255.
10. Van Ingelgem, Y., Vandendael, I., Van den Broek, D., Hubin, A., & Vereecken, J. (2007). Influence of laser surface hardening on the corrosion resistance of martensitic stainless steel. *Electrochimica Acta*, 52(27), 7796-7801.
11. Colaço, R., & Vilar, R. (2004). Stabilisation of retained austenite in laser surface melted tool steels. *Materials Science and Engineering: A*, 385(1-2), 123-127.
12. Steyer, P., Valette, S., Forest, B., Millet, J. P., Donnet, C., & Audouard, E. (2006). Surface modification of martensitic stainless steels by laser marking and its consequences regarding corrosion resistance. *Surface engineering*, 22(3), 167-172.
13. Chen, X., Gussev, M., Balonis, M., Bauchy, M., & Sant, G. (2021). Emergence of micro-galvanic corrosion in plastically deformed austenitic stainless steels. *Materials & Design*, 203, 109614.
14. Yilbas, B. S, and Shahzada Zaman Shuja. *Laser Surface Processing and Model Studies*. Springer, 2013

15. Ion, J. C., Shercliff, H. R., & Ashby, M. F. (1992). Diagrams for laser materials processing. *Acta metallurgica et materialia*, 40(7), 1539-1551.
16. Al-Sayed, S. R., Hussein, A. A., Nofal, A. A., Hassab Elnaby, S. I., & Elgazzar, H. (2017). Characterization of a laser surface-treated martensitic stainless steel. *Materials*, 10(6), 595.
17. Lo, K. H., Cheng, F. T., & Man, H. C. (2003). Laser transformation hardening of AISI 440C martensitic stainless steel for higher cavitation erosion resistance. *Surface and Coatings Technology*, 173(1), 96-104.
18. Moradi, M., Ghorbani, D., Moghadam, M. K., Kazazi, M., Rouzbahani, F., & Karazi, S. (2019). Nd: YAG laser hardening of AISI 410 stainless steel: Microstructural evaluation, mechanical properties, and corrosion behavior. *Journal of Alloys and Compounds*, 795, 213-222.
19. Mahmoudi, B., Torkamany, M. J., Aghdam, A. S. R., & Sabbaghzade, J. (2010). Laser surface hardening of AISI 420 stainless steel treated by pulsed Nd: YAG laser. *Materials & Design (1980-2015)*, 31(5), 2553-2560.
20. Vilar, R., Colaco, R., & Almeida, A. (1995). Laser surface treatment of tool steels. *Optical and quantum electronics*, 27(12), 1273-1289.
21. Maharjan, N., Zhou, W., Zhou, Y., & Wu, N. (2018). Decarburization during laser surface processing of steel. *Applied Physics A*, 124(10), 1-9.
22. Weng, F., Chen, C., & Yu, H. (2014). Research status of laser cladding on titanium and its alloys: A review. *Materials & Design*, 58, 412-425.
23. Yap, C. Y., Chua, C. K., Dong, Z. L., Liu, Z. H., Zhang, D. Q., Loh, L. E., & Sing, S. L. (2015). Review of selective laser melting: Materials and applications. *Applied physics reviews*, 2(4), 041101.
24. Mahamood, R. M., Akinlabi, E. T., Shukla, M., & Pityana, S. (2013). Scanning velocity influence on microstructure, microhardness and wear resistance performance of laser deposited Ti6Al4V/TiC composite. *Materials & design*, 50, 656-666.
25. Svenungsson, J., Choquet, I., & Kaplan, A. F. (2015). Laser welding process—a review of keyhole welding modelling. *Physics procedia*, 78, 182-191.
26. Steen, W. M., & Mazumder, J. (2010). *Laser material processing*. Springer science & business media.
27. Brown, M. S., & Arnold, C. B. (2010). Fundamentals of laser-material interaction and application to multiscale surface modification. In *Laser precision microfabrication* (pp. 91-120). Springer, Berlin, Heidelberg.
28. Dowden, J. (2009). The theory of laser materials processing. *Heat and Mass Transfer in Modern Technology*, 95-128.
29. Poirier, D. R., & Geiger, G. (Eds.). (2016). *Transport phenomena in materials processing*. Springer.

30. H.J. Breukelman, *Architected Microstructures: The effect of localized laser heat treatment on the microstructure of a FeC/Ni steel*, Thesis, 2019
31. Li, C., Wang, Y., Zhan, H., Han, T., Han, B., & Zhao, W. (2010). Three-dimensional finite element analysis of temperatures and stresses in wide-band laser surface melting processing. *Materials & Design*, 31(7), 3366-3373.
32. Sobamowo, G. M., Jaiyesimi, L., & Waheed, A. O. (2017). Transient three-dimensional thermal analysis of a slab with internal heat generation and heated by a point moving heat source. *Iranian Journal of Mechanical Engineering Transactions of the ISME*, 18(1), 43-64. *Mechanical Engineering Transactions of the ISME* 18.1 (2017): 43-64.
33. Bailey, N. S., Tan, W., & Shin, Y. C. (2009). Predictive modeling and experimental results for residual stresses in laser hardening of AISI 4140 steel by a high power diode laser. *Surface and Coatings Technology*, 203(14), 2003-2012.
34. Hecht, J. (2010). A short history of laser development. *Applied optics*, 49(25), F99-F122.
35. Colaco, R., & R. Vilar. (1998). Effect of the processing parameters on the proportion of retained austenite in laser surface melted tool steels. *Journal of materials science letters* 17.7 (1998): 563-567.
36. Zanzarin, S. (2015). *Laser Cladding with metallic powders* (Doctoral dissertation, University of Trento).
37. Swartzendruber, L. J., Itkin, V. P., & Alcock, C. B. (1991). The Fe-Ni (iron-nickel) system. *Journal of phase equilibria*, 12(3), 288-312.
38. Capdevila, C., FG, C., & De Andrés, C. G. (2002). Determination of Ms temperature in steels: A Bayesian neural network model. *ISIJ international*, 42(8), 894-902.
39. Porter, David A., and Kenneth E. Easterling. *Phase transformations in metals and alloys (revised reprint)*. CRC press, 2009.
40. Gyhlestén Back, J., & Lindgren, L. E. (2018). Modelling of the Influence of Prior Deformation of Austenite on the Martensite Formation in a Low-Alloyed Carbon Steel. In *Materials Science Forum* (Vol. 941, pp. 95-99). Trans Tech Publications Ltd.
41. Jacques, P. J. (2012). Phase transformations in transformation induced plasticity (TRIP)-assisted multiphase steels. In *Phase transformations in steels* (pp. 213-246). Woodhead Publishing.
42. Zhang, X. M., Gautier, E., & Simon, A. (1989). Martensite morphology and habit plane transitions during tensile tests for Fe-Ni-C alloys. *Acta Metallurgica*, 37(2), 477-485. Umemoto,
43. M., Yoshitake, E., & Tamura, I. (1983). The morphology of martensite in Fe-C, Fe-Ni-C and Fe-Cr-C alloys. *Journal of materials science*, 18(10), 2893-2904.
44. Sato, H., & Zaefferer, S. (2009). A study on the formation mechanisms of butterfly-type martensite in Fe-30% Ni alloy using EBSD-based orientation microscopy. *Acta materialia*, 57(6), 1931-1937.

45. Apple, C. A., & Krauss, G. (1972). The effect of heating rate on the martensite to austenite transformation in Fe-Ni-C alloys. *Acta metallurgica*, 20(7), 849-856.
46. Meshkov, Y. Y., & Pereloma, E. V. (2012). The effect of heating rate on reverse transformations in steels and Fe-Ni-based alloys. In *Phase transformations in Steels* (pp. 581-618). Woodhead Publishing.
47. Beverskog, B., & Puigdomenech, I. (1996). Revised pourbaix diagrams for iron at 25–300 C. *Corrosion Science*, 38(12), 2121-2135.
48. McCafferty, E. (2010). *Introduction to corrosion science*. Springer Science & Business Media.
49. Revie, R. W. (Ed.). (2011). *Uhlig's corrosion handbook* (Vol. 51). John Wiley & Sons.
50. Klapper, H. S., Zadorozne, N. S., & Rebak, R. B. (2017). Localized corrosion characteristics of nickel alloys: a review. *Acta Metallurgica Sinica (English Letters)*, 30(4), 296-305.
51. Popov, B. N. (2015). *Corrosion engineering: principles and solved problems*. Elsevier.
52. Loto, R. T. (2013). Pitting corrosion evaluation of austenitic stainless steel type 304 in acid chloride media. *J. Mater. Environ. Sci.*, 4(4), 448-459.
53. Li, S., & Hihara, L. H. (2012). In situ Raman spectroscopic study of NaCl particle-induced marine atmospheric corrosion of carbon steel. *Journal of the Electrochemical Society*, 159(4), C147..
54. Wen, C., Tian, Y., Wang, G., Hu, J., & Deng, P. (2016). The Influence of Nickel on Corrosion Behavior of Low Alloy Steel in a Cyclic Wet-dry Condition. *International Journal of Electrochemical Science*, 11(5), 4161-4173.
55. Konishi, H., Yamashita, M., Uchida, H., & Jun, I. M. (2005). Characterization of rust layer formed on Fe, Fe-Ni and Fe-Cr alloys exposed to Cl-rich environment by Cl and Fe K-Edge XANES measurements. *Materials transactions*, 46(2), 329-336.
56. Esmailzadeh, S., Aliofkhaezai, M., & Sarlak, H. (2018). Interpretation of cyclic potentiodynamic polarization test results for study of corrosion behavior of metals: A review. *Protection of metals and physical chemistry of surfaces*, 54(5), 976-989.
57. Zhang, H., Zhang, C. H., Wang, Q., Wu, C. L., Zhang, S., Chen, J., & Abdullah, A. O. (2018). Effect of Ni content on stainless steel fabricated by laser melting deposition. *Optics & Laser Technology*, 101, 363-371.
58. Yau, Y. H., and M. A. Streicher. "Galvanic corrosion of duplex FeCr-10% Ni alloys in reducing acids." *Corrosion* 43.6 (1987): 366-373.
59. Andersson, J. O., Helander, T., Höglund, L., Shi, P., & Sundman, B. (2002). Thermo-Calc & DICTRA, computational tools for materials science. *Calphad*, 26(2), 273-312.
60. Hunkeler, F., A. Krolikowski, and H. Böhni. "A study of the solid salt film on nickel and stainless steel." *Electrochimica acta* 32.4 (1987): 615-620.

61. Sente Software Ltd., *JMatPro4.0 [Computer software]*, 2001.
62. Sun, S., M. Brandt, and M. Easton. "Powder bed fusion processes: An overview." *Laser additive manufacturing* (2017): 55-77.
63. Xiao, R., & Zhang, X. (2014). Problems and issues in laser beam welding of aluminum–lithium alloys. *Journal of Manufacturing Processes*, 16(2), 166-175.
64. Schneider, C. A., Rasband, W. S., & Eliceiri, K. W. (2012). NIH Image to ImageJ: 25 years of image analysis. *Nature methods*, 9(7), 671-675.
65. Sato, H., & Zaeferrer, S. (2009). A study on the formation mechanisms of butterfly-type martensite in Fe–30% Ni alloy using EBSD-based orientation microscopy. *Acta materialia*, 57(6), 1931-1937.
66. Zhang, B., Fenineche, N. E., Liao, H., & Coddet, C. (2013). Microstructure and magnetic properties of Fe–Ni alloy fabricated by selective laser melting Fe/Ni mixed powders. *Journal of Materials Science & Technology*, 29(8), 757-760.
67. Glicksman, M. E. (2012). Mechanism of dendritic branching. *Metallurgical and Materials Transactions A*, 43(2), 391-404.
68. Yuan, P., & Gu, D. (2015). Molten pool behaviour and its physical mechanism during selective laser melting of TiC/AlSi10Mg nanocomposites: simulation and experiments. *Journal of Physics D: Applied Physics*, 48(3), 035303.
69. Le, T. N., & Lo, Y. L. (2019). Effects of sulfur concentration and Marangoni convection on melt-pool formation in transition mode of selective laser melting process. *Materials & Design*, 179, 107866
70. Shen, H., Yan, J., & Niu, X. (2020). Thermo-fluid-dynamic modeling of the melt pool during selective laser melting for AZ91D magnesium alloy. *Materials*, 13(18), 4157.
71. McNallan, M. J., & Debroy, T. (1991). Effect of temperature and composition on surface tension in Fe-Ni-Cr alloys containing sulfur. *Metall. Trans. B*, 22(4), 557-560.
72. Chua, C. K., Wong, C. H., & Yeong, W. Y. (2017). *Standards, quality control, and measurement sciences in 3D printing and additive manufacturing*. Academic Press.
73. Krauss Jr, G. (1963). Fine structure of austenite produced by the reverse martensitic transformation. *Acta Metallurgica*, 11(6), 499-509.
74. Chiba, T., Shirazi, H., Miyamoto, G., & Furuhaara, T. (2017). Grain refinement by cyclic displacive forward/reverse transformation in Fe-high-Ni alloys. *Metallurgical and Materials Transactions A*, 48(9), 4204-4210.
75. Alaei, A., Jafarian, H., & Eivani, A. R. (2016). Observation austenite memory and significant enhancement of tensile properties during cyclic reverse martensite transformation in a Fe-Ni-C TRIP steel. *Materials Science and Engineering: A*, 676, 342-350.
76. Shirazi, H., Miyamoto, G., Nedjad, S. H., Chiba, T., Ahmadabadi, M. N., & Furuhaara, T. (2018). Microstructure evolution during austenite reversion in Fe-Ni martensitic alloys. *Acta Materialia*, 144, 269-280.

77. Nakada, N., Fukagawa, R., Tsuchiyama, T., Takaki, S., Ponge, D., & Raabe, D. (2013). Inheritance of dislocations and crystallographic texture during martensitic reversion into austenite. *ISIJ international*, 53(7), 1286-1288.
78. Sandee, I. J. (1942). Forms of grain boundaries as may appear on primary recrystallization of deformed metals. *Physica*, 9(7), 741-754.
79. Condit, D. O. (1972). Potentiodynamic polarization studies of Fe-Ni binary alloys in sulfuric acid solution at 25 C. *Corrosion Science*, 12(5), 451-462.
80. Sherif, E. S. M., Erasmus, R. M., & Comins, J. D. (2010). In situ Raman spectroscopy and electrochemical techniques for studying corrosion and corrosion inhibition of iron in sodium chloride solutions. *Electrochimica Acta*, 55(11), 3657-3663
81. Soltis, J. (2015). Passivity breakdown, pit initiation and propagation of pits in metallic materials—review. *Corrosion Science*, 90, 5-22.
82. Shi, Y., Yang, B., & Liaw, P. K. (2017). Corrosion-resistant high-entropy alloys: A review. *Metals*, 7(2), 43..
83. Korkh, M. K., Korkh, Y. V., Rigmant, M. B., Kazantseva, N. V., & Vinogradova, N. I. (2016). Using Kelvin probe force microscopy for controlling the phase composition of austenite–martensite chromium–nickel steel. *Russian Journal of Nondestructive Testing*, 52(11), 664-672.
84. Shi, L., Song, Y., Zhao, P., Wang, H., Dong, K., Shan, D., & Han, E. H. (2020). Variations of galvanic currents and corrosion forms of 2024/Q235/304 tri-metallic couple with multivariable cathode/anode area ratios: Experiments and modeling. *Electrochimica Acta*, 359, 136947.
85. Qian, J., Chen, C., Yu, H., Liu, F., Yang, H., & Zhang, Z. (2016). The influence and the mechanism of the precipitate/austenite interfacial C-enrichment on the intergranular corrosion sensitivity in 310 S stainless steel. *Corrosion science*, 111, 352-361.
86. Uzun, H., & Önal, E. (2013). Mechanical properties and corrosion behaviors in 3.5% NaCl solution of grade-A and dual-phase steels welded by FCAW. *Periodicals of Engineering and Natural Sciences (PEN)*, 1(2).
87. Pistorius, P. C., & Burstein, G. T. (1992). Metastable pitting corrosion of stainless steel and the transition to stability. *Philosophical Transactions of the Royal Society of London. Series A: Physical and Engineering Sciences*, 341(1662), 531-559.
88. Bösing, I., Bobrov, I., Epp, J., Baune, M., & Thöming, J. (2020). Influence of Systematically Changed Martensite Content on the Passive Film Properties of Austenitic Stainless Steel in Neutral Electrolyte. *Int. J. Electrochem. Sci*, 15, 319-333.
89. McMurtrey, M. D., Mills, D. E., & Burns, J. T. (2019). The effect of pit size and density on the fatigue behaviour of a pre-corroded martensitic stainless steel. *Fatigue & Fracture of Engineering Materials & Structures*, 42(1), 3-18.

90. Gaberšček, M., & Pejovnik, S. (1996). Impedance spectroscopy as a technique for studying the spontaneous passivation of metals in electrolytes. *Electrochimica acta*, 41(7-8), 1137-1142.
91. Man, C., Dong, C., Liu, T., Kong, D., Wang, D., & Li, X. (2019). The enhancement of microstructure on the passive and pitting behaviors of selective laser melting 316L SS in simulated body fluid. *Applied Surface Science*, 467, 193-205.
92. Li, T., Liu, L., Zhang, B., Li, Y., & Wang, F. (2016). An investigation on the continuous and uniform thin membrane passive film formed on sputtered nanocrystalline stainless steel. *Corrosion Science*, 104, 71-83.
93. Zhang, B., & Ma, X. L. (2019). A review—Pitting corrosion initiation investigated by TEM. *Journal of Materials Science & Technology*, 35(7), 1455-1465.
94. Nasrazadani, S., & Hassani, S. (2016). Modern analytical techniques in failure analysis of aerospace, chemical, and oil and gas industries. *Handbook of Materials Failure Analysis with Case Studies from the Oil and Gas Industry*, 39-54.
95. Rayment, T., Davenport, A. J., Dent, A. J., Tinnes, J. P., Wiltshire, R. J., Martin, C., ... & Mosselmans, J. F. W. (2008). Characterisation of salt films on dissolving metal surfaces in artificial corrosion pits via in situ synchrotron X-ray diffraction. *Electrochemistry Communications*, 10(6), 855-858.
96. Soltis, J. (2015). Passivity breakdown, pit initiation and propagation of pits in metallic materials—review. *Corrosion Science*, 90, 5-22.
97. Hunkeler, F., A. Krolkowski, and H. Böhni. "A study of the solid salt film on nickel and stainless steel." *Electrochimica acta* 32.4 (1987): 615-620.